Spectroscopic investigation of catalytic intermediates of the Chlorite Dismutase from *Azospira oryzae*

– a treasure hunt –

by Julia Püschmann

In partial fulfilment of the requirements for the degree of Master of Science in Life Science and Technology, Technical University of Delft

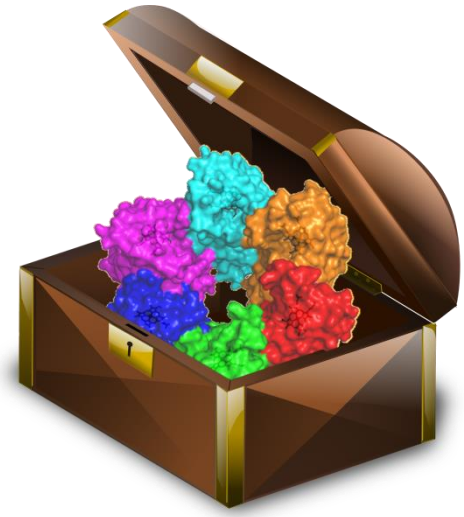

Student number: 4742605

Daily supervisor: Dr. Durga Mahor

Thesis committee: Dr. P. L. Hagedoorn, thesis supervisor
Prof. W. R. Hagen
Dr. M. Pabst

Delft, 17.06.2019

This page intentionally left blank

Abstract

Anthropogenic activities like chemical industries are releasing chlorinated species, such as perchlorate (ClO_4^-) or chlorite (ClO_2^-), into the environment. These substances are toxic and difficult to treat in the wastewater. However, nature offers a way to solve this problem. Perchlorate-respiring bacteria possess an enzyme, namely called Chlorite dismutase (Cld). It can detoxify chlorite (ClO_2^-) - a by-product of the perchlorate respiration - to chloride (Cl^-) and molecular oxygen (O_2). Therefore, it is interesting to characterise Clds in more detail to resolve its reaction mechanism and to investigate its potential for wastewater treatment.

Cld from *Azospira oryzae* (*Ao*Cld) has been produced in substantial amounts by improving the following cultivation conditions: inducer concentration, cultivation temperature, and harvest time point. After extensive removal of imidazole, a contaminant after purification of the recombinant enzyme, the yield of pure *Ao*Cld was increased 13-fold. Furthermore, spectral investigations showed that *Ao*Cld is a highly photo-sensitive enzyme when being exposed to a Xenon arc lamp. The kinetic properties of *Ao*Cld were found to be strongly pH and buffer dependent. The Good's buffer reduced the activity of *Ao*Cld by two orders of magnitude. Steady-state kinetic analysis of *Ao*Cld at pH 7 showed a K_m-value of 276 µM and a k_{cat} of $5.2 \cdot 10^3$ s^{-1}.

To resolve the reaction mechanism, pre-steady-state experiments were performed with a microsecond continuous flow UV-Vis spectrophotometer (Nanospec) and a microsecond freeze-hyperquenching device (MHQ). To identify putative catalytic intermediates during the reaction with the natural substrate ClO_2^-, reactions with a model substrate, peracetic acid (PAA), were conducted to assign possible unknown species later on. PAA binds rapidly to *Ao*Cld to form a Michaelis complex. The complex is cleaved heterolytically to yield Compound I with a rate constant of $2.15 \cdot 10^3$ s^{-1} which subsequently converts to Compound II with a rate of $15.13 \cdot 10^3$ s^{-1}. Measurements were repeated with ClO_2^- to find that *Ao*Cld reacts rapidly with chlorite to a putative Compound I* and subsequent to a Compound II, which returns to the ferric resting state with a rate of $51 \cdot 10^3$ s^{-1}. EPR spectroscopy revealed transient high spin and low spin signals as well as two different protein radical species.

This work presents new and direct evidence for transient high valent heme species during the reaction mechanism of an interesting enzyme, which can be applied for the bioremediation of chlorite.

Table of contents

List of abbreviations

*Ao*Cld	Chlorite dismutase from *Azospira oryzae*
BSA	bovine serum albumin
Bis-Tris	Bis(2-hydroxyethyliminotris)
Cld	Chlorite dismutase
Cpd I	Compound I
Cpd II	Compound II
CT	charge transfer
CV	column volume
cyt c	cytochrome c
*Da*Cld	Chlorite dismutase from *Dechloromonas aromatica*
E. coli	*Escherichia coli*
EPR	electron paramagnetic resonance
ES	enzyme-substrate complex or Michaelis complex
HEPES	N-(2-Hydroxyethyl)piperazine-N'-(ethanesulfonic)
HRP	Horseradish peroxidase
*Id*Cld	Chlorite dismutase from *Ideonella dechloratans*
IMAC	immobilised metal ion affinity chromatography
IPTG	isopropyl β-D-1-thiogalactopyranoside
kbar	kilobar
k_{cat}	turnover number [s^{-1}]
k_{cat}/K_m	catalytic efficiency [M^{-1} s^{-1}]
kDa	kilodalton
K_m	Michaelis-Menten constant [µM]
KPi	potassium phosphate buffer
LB	Lysogeny broth
MES	2-(N-Morpholino)ethanesulfonic acid
MHQ	microsecond freeze-hyperquenching device
Milli-Q	double distilled water
MOPS	3-(N-Morpholino)propanesulfonic acid
Nanospec	Nanosecond spectrophotometer
*Nd*Cld	Chlorite dismutase from *Candidatus Nitrospira defluvii*
*Nw*Cld	Chlorite dismutase from *Nitrobacter winogradskyi*
PAA	peracetic acid
Rz	Reinheitszahl
SDS	Sodium dodecyl sulfate-polyacrylamide gel electrophoresis
SVD	Singular Value Decomposition
TB	Terrific broth
UV-Vis	Ultraviolet-visible
v_{max}	maximum velocity

1 Introduction

1.1 Contamination of water with chlorinated species

Chlorinated species, like perchlorate (ClO_4^-), chlorate (ClO_3^-), or chlorite (ClO_2^-), are known to contaminate waste, soil, and even drinking water since 1980 [1-5]. These contaminants are a hazard to our health, as these species are strong oxidants. Chlorinated species cause oxidative damage to the red blood cells [4]. Especially, perchlorate inhibits the iodine uptake in the thyroid, lowering the thyroid hormone production, which is contributing to hyperthyroidism [6]. These chlorinated species occur, however, only rarely in nature [2]. For example, the Chilean ore mineral deposit contains only 0.03% chlorite compared to its total mass [7].

Anthropogenic activities mainly release these contaminants into the environment, as they are used in herbicides, rocket fuel, disinfectants, pyrotechnics, lubricating oil, and bleaching agents used in the textile, pulp, or paper industries [8, 9]. Chlorine dioxide is used to disinfect water, which contributes to high levels of chlorite and chlorate in drinking water, as chlorine dioxide decomposes into these two species [5].

Current methods to remove chlorinated species include ionic exchange columns, activated carbon, or chemical reduction. These methods are: inefficient, expensive, and environmental unfriendly [2]. It is, therefore, essential to remove these hazardous substances more effectively. This can be achieved by using milder and non-polluting methods, such as enzymatic remediation through a chlorite dismutase.

1.2 Chlorite Dismutase

Nature offers us a way to remove chlorite – one of the contaminating chlorine species. The enzyme chlorite dismutase (Cld, EC 1.13.11.49) detoxifies chlorite (ClO_2^-) to harmless chloride (Cl^-) and molecular oxygen (O_2). Clds are found in perchlorate-respiring bacteria. Perchlorate-respiring bacteria use perchlorate (ClO_4^-/Cl^- $E°$ = 1.287 V) or chlorate (ClO_3^-/Cl^- $E°$ = 1.03 V) as their sole electron acceptor during respiration [3, 10, 11]. Perchlorate is reduced to chlorate and subsequently to chlorite by another enzyme, (per)chlorate reductase (Figure 1-1).

The end product of this perchlorate respiration – chlorite – is toxic to the cell [1]. It is, therefore, essential for the microorganism to possess a detoxifying enzyme. A unique O=O bond is formed during the conversion of ClO_2^- to Cl^- and O_2 (Figure 1-1). An O=O bond formation has only been reported for the water-splitting reaction of the oxygen-evolving manganese cluster in photosystem II [12].

Clds are chlorite O_2-lyases present in many bacterial and archaeal phyla, like Proteobacteria, Cyanobacteria, and Nitrospirae [13-15]. Thus, Cld exists not only in perchlorate-reducing bacteria, like *Azospira oryzae* (GR-1) [16], *Dechloromonas aromatica* [17], or *Ideonella dechloratans* [18], where chlorite is produced during their metabolism; but Cld-like enzymes also occur in nitrite-oxidising bacteria, like *Candidatus Nitrospira defluvii* [13] and *Nitrobacter winogradskyi* [19].

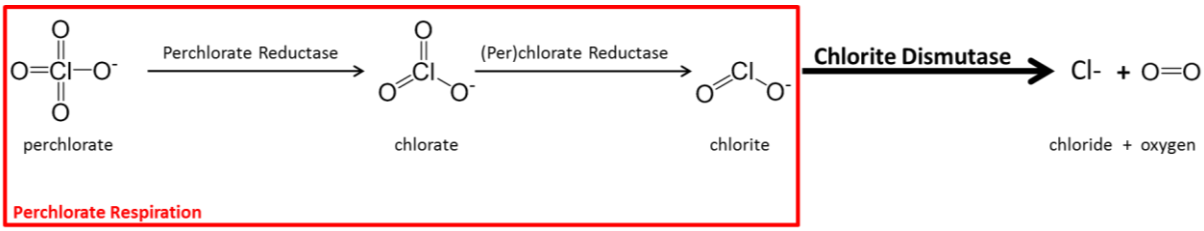

Figure 1-1. Conversion of perchlorate (ClO_4^-) to chloride (Cl^-) via (per)chlorate respiration (red box) and the enzyme chlorite dismutase in (per)chlorate-respiring bacteria.

These ancient enzymes are divided into two clades according to their sequence length. Clade I includes the “long Clds” with a heme-free N-terminal and a heme b containing C-terminal ferredoxin-like fold. For example, Clds from *Dechloromonas aromatica* (*Da*Cld) [20], *Candidatus Nitrospira defluvii* (*Nd*Cld) [14], and *Azospira oryzae* strain GR-1 (*Ao*Cld) [21] are categorised as long Clds. Clds belonging to Clade I crystallise multimeric as pentamers [14, 20] or hexamers [21]. Clade II are “short Clds” with the heme b containing C-terminal domain, which includes the dimeric Cld from *Nitrobacter winogradskyi* (*Nw*Cld) [19].

The crystal structures [14, 19-21] of all those Clds are currently investigated to discover enzymatic properties and to solve the reaction mechanism of detoxifying chlorite. *Ao*Cld was chosen for this project to investigate the reaction mechanism further.

1.3 Chlorite Dismutase from *Azospira oryzae* (*Ao*Cld)

Azospira oryzae strain GR-1, a facultative anaerobically living β-proteobacterium found in the soil [10], is a perchlorate-respiring bacterium (section 1.2). Its chlorite dismutase (*Ao*Cld) was the first Cld discovered in activated sludge of a wastewater treatment plant in 1996 [16].

*Ao*Cld is a homopentamer in solution and crystallises as a hexamer (Figure 1-2). Each monomer contains a protoporphyrin IX (heme b), has a size of 28 kDa, and is catalytic active. The ferric iron (Fe^{3+}) is positioned in the centre of the porphyrin ring, which is coordinated by an axial histidine (His170) [21]. The sixth ligand position can be taken by a water molecule [19, 22] or it is vacant for the anionic substrate, chlorite (ClO_2^-). In the resolved crystal structure (Figure 1-2) a thiocyanate (SCN^-) was bound to the iron, which was used as a ligand to crystallise the protein [21, 23].

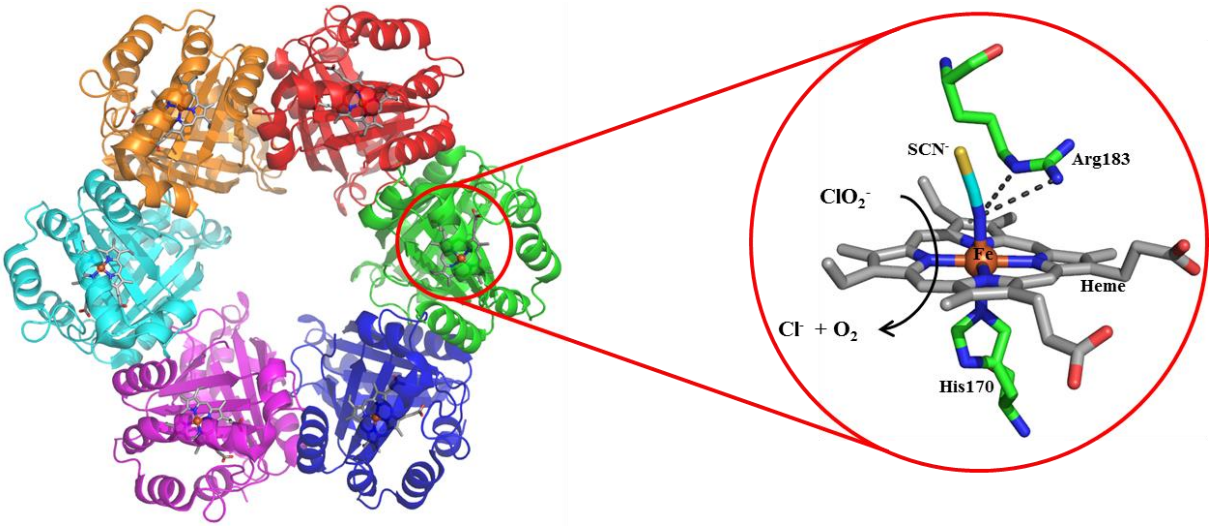

Figure 1-2. The overall crystal structure of *Ao*Cld and close-up view of the active site catalysing the conversion of ClO_2^-. The hexamer is coloured by chain and the hemes are shown in grey. The distal arginine (Arg183) and proximal histidine (His170) are coloured by atom (green). Thiocyanate (SCN^-) was used for crystallisation purposes and is coloured by atom (cyan). PDB accession code: 2VXH. Figures were generated using PyMOL (http://www.pymol.org/).

The heme cavity of *Ao*Cld (Figure 1-2) has a distal charged arginine (Arg183) which is conserved in Clds and adopts a so-called “in” position (guanidinium group pointing towards the heme group) or “out” position (guanidinium group pointing towards the entry of the substrate channel) [21]. Some Cld studies [24, 25] showed that this conserved Arg is catalytically important, as it might help facilitate the binding of ClO_2^- and the stabilisation of a potential reaction intermediate (see below).

Reaction Mechanism

With structural data available, research groups have proposed different reaction mechanisms (Figure 1-3) on how the enzyme can disproportionate ClO_2^- to Cl^- and O_2. Researchers agree that the substrate (ClO_2^-) binds to the ferric iron resting state to form a Fe(III)-chlorite complex or Michaelis complex (Fe(III)-$OClO^-$) (Figure 1-3). The subsequent catalytic steps are not established. Isotope-labelling studies [22, 26, 27] already showed that both oxygen atoms in O_2 originated from one chlorite molecule (ClO_2^-). Therefore, the first assumption (mechanism I) can be excluded.

The Michaelis complex could either be cleaved heterolytic (mechanism II) to form hypochlorite (ClO^-) and a high valent oxo-ferryl (Fe(IV)=O) species with a cation radical on the porphyrin ring (Compound I); or the Michaelis complex could be cleaved homolytic (mechanism IV) to form chlorine monoxide ($ClO^\cdot$) and a neutral high valent oxo-ferryl (Fe(IV)=O) species (Compound II). These reaction intermediates (either hypochlorite or chlorine monoxide) attack the ferryl oxygen in a rebound step (Figure 1-3), yielding Fe(III)-peroxyhypochlorite (Fe(III)-$OOCl^-$). The products, Cl^- and O_2, are released after this rebound step and the ferric resting state is restored (Figure 1-3) [28]. DuBois *et al.* claimed to have found evidence for mechanism II (heterolytic cleavage) for *Da*Cld [26, 29]; whereas Schaffner *et al.* claimed to have found evidence for mechanism IV (homolytic cleavage) for the Cld of *Cyanothece* sp. [22].

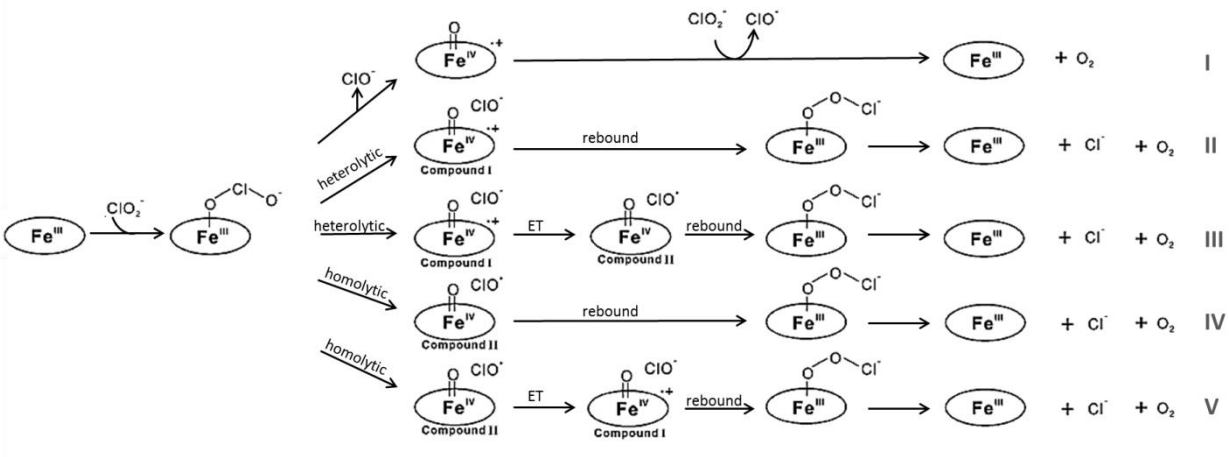

Figure 1-3. Overview of previously proposed mechanisms for the disproportionation of chlorite by Clds. ET – marks the electron transfer between the porphyrin ring and the reaction intermediate (hypochlorite or chlorine monoxide). Adapted from [30].

It is, furthermore, proposed that Compound I (mechanism III) or Compound II (mechanism V) is formed first which converts rapidly to the other oxo-ferryl species via an electron transfer step between the porphyrin ring and the reaction intermediate (hypochlorite or chlorine monoxide). The high valent heme species subsequently transforms back to the ferric resting state. A computational study from Keith *et al.*, as

well as Su and Chen examined possible transition states of *Ao*Cld for the reaction with chlorite [31, 32]. They concluded the formation of hypochlorite, and therefore Compound I, is less energetically favourable than the generation of chlorine monoxide (plus Compound II). Chlorine monoxide, moreover, is a more reactive species than hypochlorite [32]. According to their data, the researchers expect a homolytic cleavage as the first step of the reaction (mechanism IV or V).

Nonetheless, mechanisms II to V may be valid, but no research team has presented direct evidence favouring any reaction mechanism with the real substrate chlorite. Most groups investigated a possible mechanism with an artificial substrate, peracetic acid (PAA), from which it is known to chemically react with the heme cofactor to form Compound I and Compound II [33]. Similarly, peroxidases are chemically modified with hydrogen peroxide or organic peroxidases to study Compound I and II formations [34-36]. Attempts to propose a mechanism with the natural substrate ClO_2^- failed, because the overall reaction of Cld and ClO_2^- is too fast.

*Ao*Cld, for example, has a turnover number (k_{cat}) of 1200 s^{-1} at pH 7.2 in KPi buffer [16, 21, 37], meaning the reaction is completed in less than a millisecond (1 ms). The Cld from *Magnetospirillum* sp. can even complete its reaction in 0.025 ms (or 25 µs), because it exhibits a k_{cat} of 40,000 s^{-1} at pH 6.1 in KPi buffer [38]. Thus, Clds are fast enzymes, which cannot be studied with conventional steady-state methods to unravel their complete reaction mechanism. To overcome this problem, we will use microsecond timescale pre-steady-state methods (section 1.4.2) to find direct evidence for transient catalytic intermediates and suggest a possible reaction mechanism for *Ao*Cld ourselves.

1.4 Theoretical background information for this work

To understand the underlying principles used for discussion in chapter 3 and chapter 4, some pre-steady-state theory and its methods as well as EPR basics will be elucidated in this section.

1.4.1 From steady-state to pre-steady-state assumption

In an enzymatic reaction, the enzyme (E) reacts with a substrate (S) to form an enzyme-substrate-complex (ES), which converts into a product (P) and the enzyme (Figure 1-4). For analysing the kinetics of an enzyme, researchers use the idea applied in the Michaelis-Menten equation [39] that after an initial burst phase all enzyme molecules occur in an ES complex (Michaelis complex). The concentration of ES remains the same until a significant amount of substrate has been consumed. This principle is called steady-state [40].

Figure 1-4. Enzyme kinetics equation with E – enzyme, S – substrate, ES – enzyme-substrate complex, P – product, k_1, k_{-1}, k_2 – rate constants.

Steady-state measurements, however, provide us only with information about the rate determining step of the reaction or more precise: the step that accounts for the greatest part of the overall reaction (Figure 1-4). For identifying a complete reaction mechanism it is, therefore, essential to resolve all possible steps involved, including the fast ones [40]. This becomes clear in a Gibbs energy diagram (Figure 1-5). The ES complex decays to multiple intermediates until the final product is released (Figure 1-5).

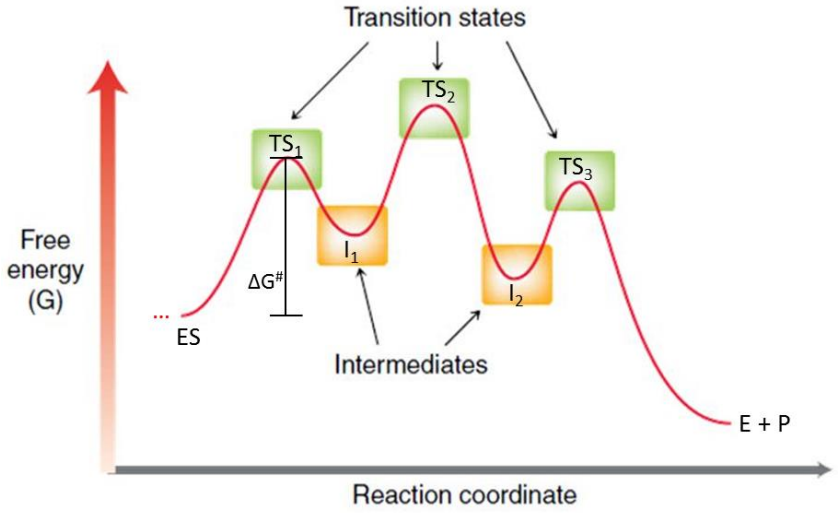

Figure 1-5. Transition states (TS) diagram for an enzyme catalysed reaction with multiple intermediates (I). $\Delta G^{\#}$ gives the slowest step or rate-determining step in the overall reaction from ES to E + P. Adapted from [41].

These intermediates are undetectable with standard steady-state experiments because the intermediates are formed and broken down faster than the total rate of the enzyme; steady-state experiments, however, can only measure the total reaction rate.

Another drawback of steady-state measurement is that usual methods take seconds or more to measure. With fast reactions, which can be completed in less than a second, this is too slow. Furthermore, with steady-state techniques, we observe the effect on reactants (decrease of substrate or increase of product) instead of the enzyme itself. Pre-steady-state or transient kinetics covers the time of a reaction before it reaches steady-state. With specialised methods (section 1.4.2), individual

fast and slow steps of a mechanism can be detected, as we are observing the enzyme itself with spectroscopic techniques to obtain rate constants to complete the picture of the enzyme mechanism [40, 42].

The equation of Figure 1-4 is rewritten to include potential intermediates (Figure 1-6). In this equation, k_1 represents a second-order rate constant with a unit in M^{-1} s^{-1}, because the rate is proportional to the product of two concentrations ([E] and [S]).

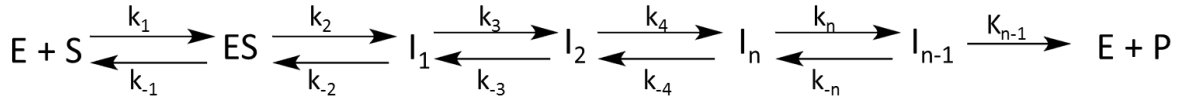

Figure 1-6. Enzyme kinetics equation with pre-steady-state assumption with E – enzyme, S – substrate, ES – enzyme-substrate complex, I – intermediate, P – product, k_1, k_{-1}, k_2, …, k_{n-1} – rate constants.

The decay of one intermediate (I) to another is considered as a first-order reaction with first-order rate constants (k_2, k_3, k_4, …) given in s^{-1}. The rate dependents only on one concentration ($[I_1]$, $[I_2]$, $[I_3]$, $[I_4]$, …) [40, 42]. Practically, it is easier to measure first-order reactions; however, the first step of every enzyme reaction is a second-order reaction. This problem can be circumvented when [S] >> [E], therefore [S] remains constant and only [E] changes throughout the reaction. We are now able to follow a single exponential decay with a pseudo first-order rate constant, called k_{obs}. With [S] in large excess, the substrate-binding step is fast and in principle, all enzyme molecules are in an ES complex and we can observe the subsequent decay of intermediates [40, 42]. To monitor the rapid conversion of intermediates, special equipment is needed.

1.4.2 Pre-steady-state methods

Transient kinetic methods can be divided into flow techniques (millisecond timescale, ms): including stopped, continuous, or quenched flow devices and hydrodynamic focussing; or relaxation techniques: including pressure or temperature jump (microsecond timescale, µs); or time-resolved X-ray crystallography and ultrasonic methods (nanosecond timescale, ns), as well as flash photolysis (femtosecond timescale, fs) [40].

It is crucial for pre-steady-state measurements that enzyme and substrate solution are mixed rapidly to measure in time regimes below a second. Rapid mixing can be achieved with mixers that create turbulent flow, but also high linear flow rates ensure the complete immediate mixing of the two solutions [42, 43]. This section will cover a brief overview of stopped, continuous, and quenched flow methods as these are applied later on (section 3.3).

Stopped-Flow

The most commonly used equipment for pre-steady-state kinetic studies is the stopped-flow. A drive pushes two syringes, containing the substrate and the enzyme, simultaneously. After leaving the mixing device (T-mixer), the mixed solution passes an observation cell and fills the stop syringe. The stop syringe hits a switch, which stops the flow and activates the spectroscopic measurement in the observation cell (Figure 1-7). The dead time of classical stopped-flow instruments, or the time necessary for the solution to enter the observation cell after the mixer, is 1 ms [40].

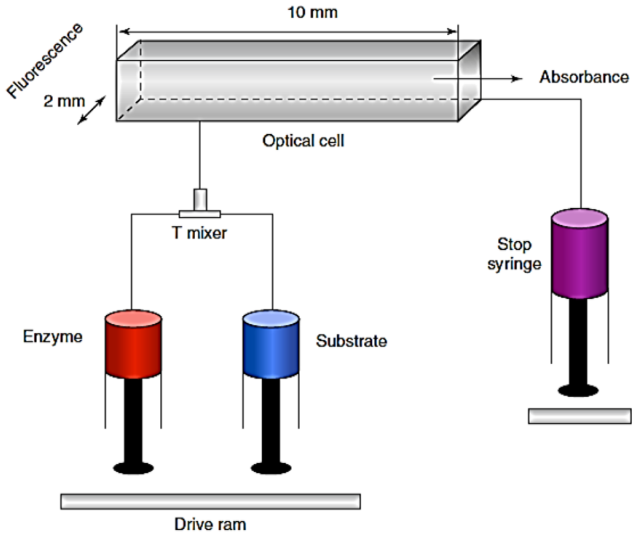

Figure 1-7. Set-up of a stopped-flow equipment used for transient kinetic experiments. A ram drives two syringes; the solutions are mixed in a T-mixer; the mixed solution fills the optical cell until the stop syringe hits the switch to stop the flow. Taken from [42].

Continuous Flow

Another flow method is applied in continuous flow equipment where enzyme and substrate are rapidly mixed and flow through an observation tube with a movable detector. The position of the detector along the tube determines the time point of the reaction. The closer the detector is positioned to the mixer, the shorter the reaction time is [40].

The dead time of this device lies within 20 µs to 100 µs. However, De Vries and co-workers [43] succeed in constructing a special four-jet tangential micro-mixer, which allows complete mixing of enzyme and substrate within a few microseconds. This mixer was used in a continuous flow instrument with a dead time of 4 µs and is called Nanosecond spectrophotometer (Nanospec). The Nanospec uses high linear flow rates, high pressures supplied by HPLC pumps, and a fast scanning monochromator [43]. 1900 UV-Vis spectra are recorded in a timeframe from 4 µs to a maximum of 2.5 ms depending on the flow rate.

A drawback of the continuous flow method is that it requires a large amount of protein because per run 1 mL of 1 mM of *Ao*Cld ($MW_{Monomer}$: 28 kDa) was needed. This leads up to 300 mg of *Ao*Cld per set of experiments (7 to 8 different substrate concentrations can be tested with this amount of enzyme).

Quenched Flow/Rapid Freezing

The third and last flow method is the quenched or rapid freezing technique. Substrate and enzyme solution are mixed rapidly in a very similar four-jet tangential micro-mixer as is used in the Nanospec. However, in this case the mixture does not enter a cuvette, but it enters an ageing loop and is sprayed through a nozzle into a cryo-medium bath, usually cooled isopentane (130 K to 140 K) or cooled liquid ethane (90 K to 120 K) (Figure 1-8) [40].

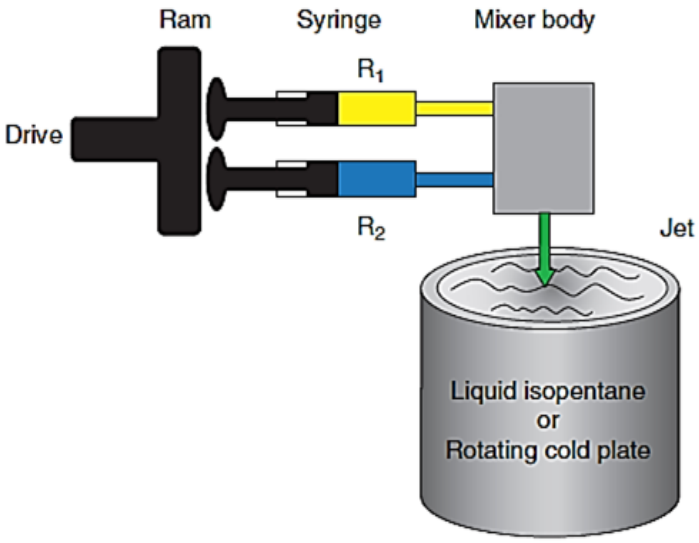

Figure 1-8. Principle set-up of rapid freezing devices and microsecond freeze-hyperquenching device (MHQ). The mixer body mixes reactant 1 (R_1) and reactant 2 (R_2). The distance (green arrow) between the mixer and the liquid isopentane (130 K to 140 K) or rotating cold plate (77 K) is variable and determines the reaction time. Taken from [42].

The mixture freezes and the reaction is quenched or stopped. The overall time, at which the reaction is quenched, can be varied by changing the length of the ageing loop before the nozzle and the distance between nozzle and cryo-medium. The minimal dead time of this equipment is 6 ms [42]. Especially the freezing time in isopentane or liquid ethane is the slowest step in the set-up. De Vries and co-workers [44, 45] succeed to decrease the dead time to 80 µs for rapid freezing devices, because they used a rotating cold plate instead of isopentane. This minimises the heat transfer and shortens the freezing time of the solution significantly. The in-house built microsecond freeze-hyperquenching device (MHQ) makes also use of the

miniaturised version of a four-jet tangential mixer and HPLC pumps as described above [42, 44, 45]. The frozen samples can be used for various investigations techniques, as low-temperature UV-Vis, EPR, or Resonance Raman spectroscopy.

1.4.3 Electron Paramagnetic Resonance (EPR) theory

The basic principles of electron paramagnetic resonance (EPR) are described in this section, as EPR is not only used to characterise the enzyme during the purification (section 3.1.2) but also to analyse the samples prepared with the MHQ to detect possible catalytic intermediates (section 3.3).

EPR is a spectroscopic method which uses microwaves to detect unpaired electrons [46, 47]. EPR can be applied as an analytical tool here native *Ao*Cld with its heme cofactor possesses ferric iron ions (Fe^{3+}) with unpaired electrons (S = 5/2). The unpaired electrons orientate themselves in spin up (higher energy state) or spin down (lower energy state) position to an external magnetic field. The X-band microwave frequency (9.4 GHz) is fixed, but the external magnetic field is increased (from 50 Gauss to 5050 Gauss) during each measurement. The increasing magnetic field causes the higher and lower energy level to split (Figure 1-9, left) until it matches the microwave radiation and the molecule absorbs the energy which the spectrometer detects [46, 47].

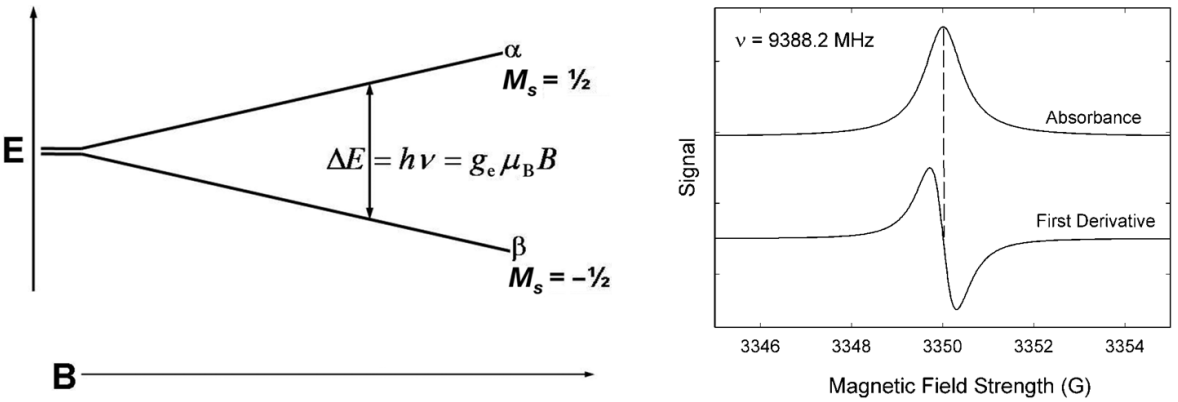

Figure 1-9. Basic EPR principles. Left: Splitting of energy levels for an electron spin (S = 1/2) in an applied magnetic field B. Taken from [46]. Right: Absorbance spectrum (top) is converted to an EPR spectrum (bottom) by taking its first derivative. Taken from [48].

The absorbance spectrum is converted to its first derivative (dX''/dB) (Figure 1-9, right). The centre of this signal in the first derivative is used to calculate the g-factor, a characteristic for every paramagnetic species. A free electron in vacuum has a g-factor of g_e = 2.00232. Since isotropic radicals may resemble a free electron, their g-factor ranges from 1.99 – 2.01 [46, 47]. Therefore, each paramagnetic transition metal ion/cofactor and radical has its characteristic EPR spectrum.

To detect potential catalytic intermediates (section 3.3), it is relevant to have comparable EPR spectra from a porphyrin π-cation radical coupled to a high valent oxo-ferryl species (Compound I) and an amino acid-based radical (Figure 1-10).

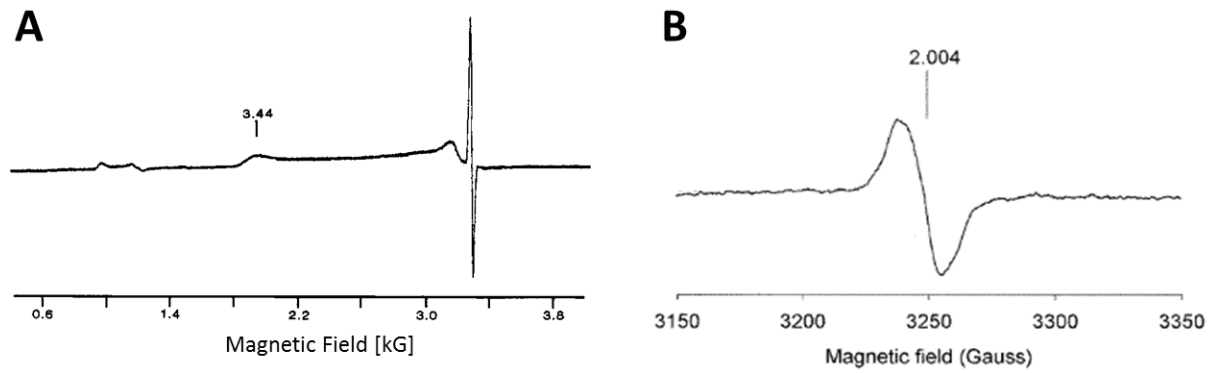

Figure 1-10. Example EPR spectra of a Compound I (A) and tyrosyl radical (B). A – Catalase from *Micrococcus lysodeikticus* was reacted with PAA and flash frozen after 30 s. Taken from [49]. B – catalase-peroxidase from *Mycobacterium tuberculosis* was reacted with PAA and flash frozen after 10 ms. Adapted from [50].

1.5 Objectives of this Master End Project

This work aimed to identify catalytic intermediates (Figure 1-3), if there are any involved, during the reaction of Cld with its natural substrate chlorite (ClO_2^-) at pH 7, with the help of established as well as in-house built pre-steady-state instruments, as described in section 1.4.2.

In order to perform these experiments, a substantial amount of enzyme (>1 gram) was necessary. To obtain as much protein as possible during the big-scale fermentation, the overexpression of the enzyme was optimised. The effect of typical cultivation parameters, like the inducer concentration or the temperature during the overexpression, was investigated. After optimisation of the enzyme expression and the large scale enzyme production (4 x 15 L), the purification protocol for *Ao*Cld was adjusted to facilitate bulk purification. The protein has to be as pure as possible, to make sure that no contaminants are binding to the active site affecting the kinetics of the enzyme, which could obscure the determination of the rate constants.

After the enzyme was successfully prepared, *Ao*Cld was characterised regarding the activity in different buffers and ionic strength to determine the reaction conditions for steady-state as well as pre-steady-state experiments. The determined kinetic parameters were used to design the pre-steady-state experiments. The goal of these experiments was to identify any catalytic intermediates and, finally, propose a reaction mechanism at pH 7 with calculated rate constants for the reaction with the unnatural substrate peracetic acid (PAA) and the natural substrate ClO_2^-.

2 Materials and Methods

2.1 Chemicals and enzymes

Peracetic acid ($C_2H_4O_3$) was obtained from Acros Organics.

Agar, tryptone, and yeast-extract were purchased from Becton, Dickson and Company.

Ascorbic acid ($C_6H_8O_6$) and dipotassium hydrogen phosphate (K_2HPO_4) were supplied by Fluka Chemika.

Citric acid ($C_6H_8O_7$), sodium chloride (NaCl) and sodium hydroxide (NaOH) were obtained from J. T. Baker.

Glycerol ($C_3H_8O_3$), imidazole, potassium dihydrogen phosphate (KH_2PO_4), and sodium acetate ($NaC_2H_3O_2$) were purchased from Merck KGaA.

Acetic acid ($C_2H_4O_2$), Bis-Tris, chloramphenicol, disodium hydrogen phosphate (Na_2HPO_4), DNase, hemin, hydrochloric acid (HCl), HEPES, kanamycin, lysozyme, magnesium sulfate ($MgSO_4$), MES, MOPS, PMSF, sodium chlorite ($NaClO_2$), sodium citrate ($Na_3C_6H_5O_7$), sodium dithionite ($Na_2S_2O_4$), and Tris-Base were obtained from Sigma-Aldrich.

IPTG was purchased from Thermo Fisher Scientific.

2.2 Preparative enzyme production

2.2.1 Cultivation and recombinant gene expression in *Escherichia coli*

Escherichia coli (*E. coli*) BL21(DE3)pLysS with a pET28a plasmid carrying the desired gene for *Ao*Cld [23], was streaked on a Lysogeny Broth (LB) agar plate (Table 2-1) containing kanamycin (50 µg mL^{-1}) and chloramphenicol (25 µg mL^{-1}) using a polypropylene inoculating loop. The culture was from a -80°C glycerol stock. The plate was incubated at 37°C for 16 hours (Thermo Scientific Heraeus Heating Oven). A single colony was picked from the LB plate to inoculate a pre-culture with 400 mL LB medium (Table 2-1) containing kanamycin (50 µg mL^{-1}) and chloramphenicol (25 µg mL^{-1}). The pre-culture was incubated at 37°C with 150 rpm for 16 hours (Eppendorf New Brunswick™ Innova® 44).

The pre-inoculum (2%) was transferred in a 15 L fermenter (Applikon) with Terrific Broth (TB) medium (Table 2-1) supplemented with TB salts (89 mM), kanamycin (50 µg $mL^{-}1$), chloramphenicol (25 µg mL^{-1}), and hemin (60 µg mL^{-1}). The fermentation broth was stirred with 750 rpm and the oxygen inflow was 5 L min^{-1}. A

few drops of Basildon antifoam were added. The recombinant gene expression was induced after the OD_{600} reached 0.5 through the addition of isopropyl β-D-1-thiogalactopyranoside (IPTG) (500 µg mL^{-1}). The cultivation temperature was reduced from 37°C to 25°C after induction. The culture was harvested 7 hours after induction. The cells were harvested by centrifugation (Sorvall™, 16770 g, 10 min, 4°C). The cell pellet was washed twice with 20 mM Tris-HCl pH 7.5, 500 mM NaCl, and 50 mM imidazole (pH 7.5). The cells were stored at -80°C until further treatment, cell lysis (section 2.2.2).

Table 2-1. The composition of the media.

Medium	Component	Medium	Component
LB	1% (w/v) NaCl 1% (w/v) tryptone 0.5% (w/v) yeast-extract	TB	0.5% (w/v) glycerol 1.2% (w/v) tryptone 2.4% (w/v) yeast-extract
LB agar	additionally 1.2% (w/v) agar	TB salts	2.31% (w/v) KH_2PO_4 12.54% (w/v) K_2HPO_4

2.2.2 Cell lysis

The cell pellet was dissolved in cell lysis buffer (Table 2-2). The re-suspended cells were homogenised with a Disperser (Homogenizer RW16 basic, IKA®-Werke) and lysed with a cell disruptor (CF 1, Constant Systems Ltd.). The cells were compressed with 1.5 kbar. To separate the cell debris from soluble proteins, the cell lysate was centrifuged (Sorvall™, 16770 g, 90 min, 4°C). The supernatant was filter sterilised (0.22 µm Steritop™ Filter, Millipore) prior to the next purification step, immobilised metal ion affinity chromatography (IMAC) (section 2.3.1).

Table 2-2. The composition of cell lysis buffer.

Component	Concentration
DNase	10 µg mL^{-1}
Imidazole pH 7.5	50 mM
Lysozyme	200 mg L^{-1}
$MgSO_4$	1 mM
NaCl	500 mM
PMSF	1 mM
Tris-HCl pH 7.5	20 mM

2.3 Preparative enzyme purification

2.3.1 Affinity chromatography

IMAC was performed, because the recombinant *Ao*Cld has an N-terminal His-tag. Therefore, a HisTrap purification on an NGC™ Chromatography System (Bio-Rad) was conducted. A 150 mL Ni Sepharose™ 6 Fast-Flow column (GE Healthcare) was used to purify ~1.5 L supernatant after cell lysis (section 2.2.2). The column was equilibrated with 3 to 4 column volumes (CV) with equilibration buffer (flow rate: 3 mL min^{-1}), see Table 2-3.

Table 2-3. The composition of the buffers used during affinity chromatography.

Solution	Component	Solution	Component
Equilibration Buffer pH 7.5	50 mM Imidazole 500 mM NaCl 20 mM Tris-HCl	Elution Buffer pH 7.5	500 mM Imidazole 150 mM NaCl 20 mM Tris-HCl

After loading of the sample with a flow rate of 0.7 mL min^{-1} overnight, the column was washed with 1.5 CV with equilibration buffer (flow rate: 3 mL min^{-1}). The protein was eluted in an increasing gradient of 4 CV from 0% to 100% elution buffer (Table 2-3), followed by 2 CV of 100% elution buffer, and a decreasing gradient from 100% to 0% elution buffer with 1 CV (flow rate: 3 mL min^{-1}). The elution fractions were pooled and stored at 4°C until the next purification step, desalting (section 2.3.2).

2.3.2 Desalting

The HisTrap purified protein was desalted in two steps. In a first step, it was desalted with HiTrap Desalting columns (GE Healthcare) using the NGC™ system (Bio-Rad). The columns were equilibrated and the protein was eluted with 20 mM Tris-HCl buffer, pH 7.5 (flow rate: 4 mL min^{-1}). In a second step, the protein solution was desalted using PD10 columns (GE Healthcare). The columns were equilibrated and the protein was eluted with 50 mM potassium phosphate buffer, pH 7. The coloured fractions were collected and stored at 4°C until the next purification step, dialysis (section 2.3.3).

2.3.3 Dialysis

The protein solution was dialysed at 5°C in 100 mM potassium phosphate buffer, pH 7, to a dilution factor of 650 with a dialysis cycle of a minimum of 8 hours. A Visking® Dialysis Tubing with a cut-off of 3.5 kDa and a diameter of 16 mm from Medicell Membranes Ltd. was used. The purified enzyme was concentrated to 8 mg mL^{-1} using an Amicon® Ultra Centrifugal Filter (Millipore) with a 30 kDa cut-off by centrifugation at 3214 g for 20 min (Eppendorf Centrifuge 5810 R). *Ao*Cld was stored at -80°C until further use.

2.4 Biochemical analysis

2.4.1 Determination of the protein concentration

The protein concentration was determined according to the Uptima BCA protein assay kit from Interchim. The measurements were performed in triplicates using a Synergy™ 2 Microplate Reader from BioTek. The calibration curve with bovine serum albumin (BSA) is shown in Figure 2-1.

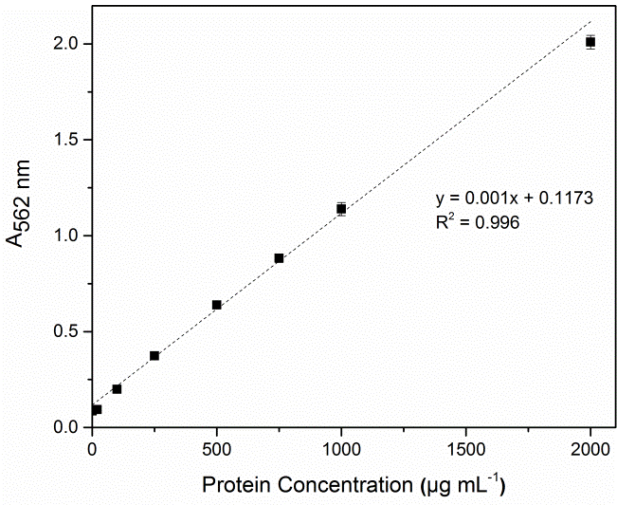

Figure 2-1. BSA calibration curve. Shown is the protein concentration in µg mL^{-1} vs. the absorption at 562 nm with standard deviations. The measurements were performed in triplicates.

2.4.2 Sodium dodecyl sulfate-polyacrylamide gel electrophoresis (SDS-PAGE)

The protein probes with a desired protein concentration were mixed with 25 µL of SDS sample buffer, which consists of 20x XT Reducing Agent (Bio-Rad) and 4x XT SDS Sample Buffer (Bio-Rad). The probes were incubated at 95°C for 10 min in an Eppendorf Thermomixer. 1 µg $µL^{-1}$ of the probes and 10 µL of the Precision Plus

Unstained Protein Standard (Bio-Rad) were loaded on a 12% Bis-Tris SDS Gel (Criterion™ XT Precast SDS Gel, Bio-Rad). The electrophoresis was performed at 200 V, 1 mA, and 300 W in 1x MES running buffer (Bio-Rad) and in a Criterion™ Blotter electrophoresis system for 45 min.

The gels were incubated with a Coomassie staining solution (Simply Blue™ SafeStain, Life Technologies) for 45 min to 60 min. The gels were, subsequently, destained in demi water.

2.4.3 Activity measurements

The activity of *Ao*Cld was, standardly, measured polarographically by a Clark-type oxygen electrode (type 5331, YSI Life Science) with 100 mM potassium phosphate buffer, pH 7, and 1 mM sodium chlorite as substrate at 20°C. The electrode was calibrated with 100% air-saturated buffer and 0% oxygen by addition of a spatula tip of sodium dithionite. The used amount of enzyme depended on the protein concentration and activity of the regarding sample. Most of the measurements were carried out with approximately 120 pM to 200 pM of *Ao*Cld (final concentration in reaction chamber). After flushing the reaction chamber with nitrogen, the reactions were initiated by injecting 15 µL to 25 µL of the enzyme solution with a gastight syringe (Hamilton®). The volumetric activity of the regarding samples were calculated with the formula described in Appendix A, equation 1.

2.4.4 UV-Vis measurements

All UV-Vis measurements were performed with a Cary 60 from Agilent Technologies spectrometer at 21°C. The spectra were, standardly, measured with 10 µM *Ao*Cld in 100 mM potassium phosphate buffer, pH 7, with a 3 mL quartz cuvette. Spectra were recorded in a wavelength range from 200 nm to 800 nm.

2.4.5 EPR

The electron paramagnetic resonance (EPR) spectra were recorded on a Bruker EMXplus spectrometer with a liquid helium cryostat at 20 K, with a microwave frequency of 9.416 GHz, a microwave power of 0.2, 20, or 79 mW, a modulation frequency of 100 kHz, and a modulation amplitude of 2, 10, or 20 G. Spectra were scanned from 50 G to 5050 G. The measured samples contained 75 µM *Ao*Cld in 200 µL 100 mM potassium phosphate buffer, pH 7, unless stated otherwise.

2.5 Pre-steady-state kinetic techniques

The rapid kinetic experiments were performed with a continuous flow and rapid freeze quenching technique. Time-resolved spectra were analysed with an in-house developed program written in LabVIEW and the KinTek software (version 8, KinTek Corp.).

2.5.1 Continuous flow experiment

With the help of a continuous flow rapid mixing UV-Vis spectrophotometric instrument, called Nanosecond spectrophotometer (Nanospec), intermediates in the microsecond timescale can be detected, because the equipment has a dead time of 4 µs [43]. The optical PMMA cell had a path length of ~100 µm and with a rapid scanning monochromator as well as a CCD camera as a detector, 1900 UV-Vis spectra have been recorded in a single run [43]. The rapid kinetic experiments were performed at 29°C, spectra were recorded from 350 nm to 650 nm, and with a total flow rate of 7 mL min^{-1} and 20 mL min^{-1} for peracetic acid (PAA) and sodium chlorite, respectively. For single mixing experiments, 1 mM of *Ao*Cld (final concentration: 500 µM) was mixed with various concentrations of PAA (1 mM to 40 mM) or various concentrations of sodium chlorite (10 mM to 50 mM). Both enzyme and PAA or sodium chlorite were dissolved in 100 mM potassium phosphate buffer, pH 7, shortly before the experiment.

2.5.2 Rapid freeze quenching technique

Microsecond freeze-hyperquenching (MHQ) is an ultrafast freeze quenching technique (section 1.4.2). An enzyme solution is rapidly mixed with the substrate solution in a tangential micro-mixer and sprayed as a free-flowing jet on a cold rotor plate [44, 45]. With this special device, rapidly mixed samples can be frozen within 80 µs [44, 45]. 1 mM of *Ao*Cld and 3 mM of PAA or 150 mM of sodium chlorite were injected in the system and mixed 1:1 with various flow rates (Table 2-4). The mixed solutions were sprayed under a vacuum (30 mbar) on a rotating plate (7122 g), which has been cooled down with liquid nitrogen. The length of the ageing loop, as well as the distance between the nozzle and the rotor plate, determine the time point at which the reaction is quenched. The technical details to prepare the samples are summarised in Table 2-4. After the samples were sprayed, liquid nitrogen was immediately poured into the rotor to keep the powder cold. The powder was scraped off the rotor plate, packed in EPR tubes, and stored at 77 K until further analysis (section 2.4.5).

Table 2-4. Parameters used in different set-ups for the MHQ.

	Reaction time [ms]	Total flow rate [mL min^{-1}]	Distance between nozzle and cold plate [mm]	Size of orifice [µm]
Set-up 1	0.097	3	8	20
Set-up 2	0.125	3	13	20
Set-up 3	0.2	3	26	20
Set-up 4	0.3	3	44	20
Set-up 5	0.8	1.8	80	20
Set-up 6	2	10	20	100
Set-up 7	15.7	10	12	100
Set-up 8	200.3	12	12	100

2.5.3 Analysis of the Nanospec data

The time-resolved spectra generated with the Nanospec are loaded into the program KinTek, which uses Singular Value Decomposition (SVD) to deconvolute the data regardless the shape and the amplitude of the spectra [51, 52]. The program produces Eigenvectors, which are observables from the data with distinct spectral information. These Eigenvectors are fitted to a model with self-chosen observables. The reaction with PAA is modelled with three intermediates and the ferric resting state enzyme as a start, which are connected through three rate constants. The reaction with chlorite is modelled from the ferric resting state to one intermediate back to the ferric resting state connected through two rate constants.

The SVD of PAA and chlorite are depicted as an example in Figure 2-2. After fitting the SVD amplitudes to the model, KinTek recalculated the data to postulate the spectra of the distinct species, which are represented in Figure 3-12 and Figure 3-18.

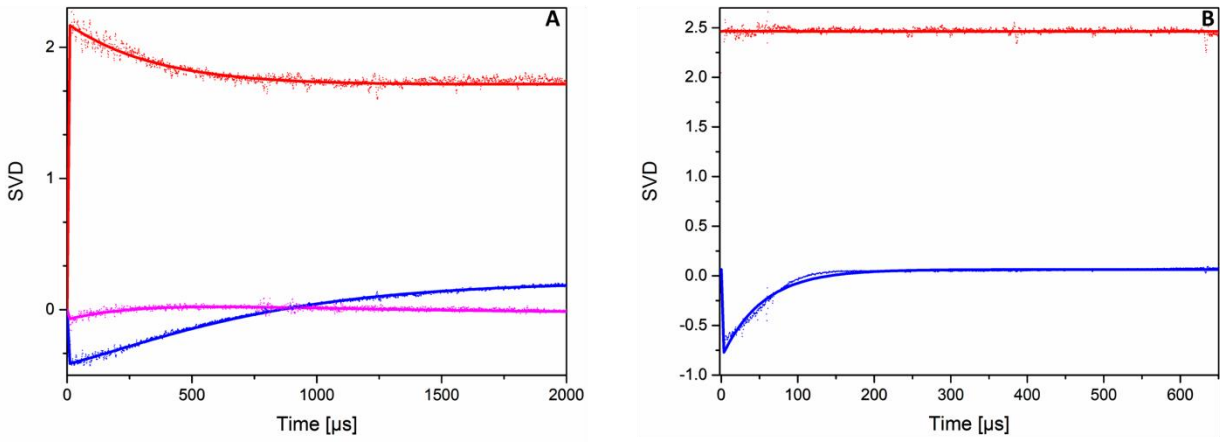

Figure 2-2. SVD analysis of the reaction of *Ao*Cld with 1 mM PAA (A) and 50 mM sodium chlorite (B). A – Data is fitted to the spectral information of the Michaelis complex (red), Compound I (blue), and Compound II (magenta). B - Data is fitted to the spectral information of the putative Compound II (red), and ferric resting state form of *Ao*Cld (blue).

2.6 Photo-effect observation

A rapid scanning photodiode array stopped-flow SX20 from Applied Photophysics was used to conduct the experiments for the observation of the photo-effect (section 3.2.2). The optical quartz cell had a path length of 10 mm and a total volume of 60 µL. For the experiments, 20 µM *Ao*Cld (final concentration: 10 µM) dissolved in 100 mM potassium phosphate buffer, pH 7, and Milli-Q were mixed rapidly in 1 ms. The enzyme was exposed to the high light energy source (Xenon arc lamp) for 0.6 s, 1 s, 30 s, 60 s, 10 min, or 15 min after each mixing event. Furthermore, the enzyme was exposed to light for 10 s and incubated without the light source for 20 min before exposing it again to light for another 10 s. This process was repeated three times with the same enzyme-water mixture. To validate the experiment and for preparation of an EPR sample, 75 µM of *Ao*Cld was incubated for 7.5 hours in another photodiode array spectrophotometer (Hewlett Packard 8453). All experiments were carried out at 20°C.

3 Results and Discussion

3.1 Enzyme preparation

Section 1.4 points out that a substantial amount of enzyme was necessary to conduct the pre-steady-state experiments. However, with the cultivation [23] and purification protocols, established prior to this master thesis, only 1 mg of protein was obtained from 1 g of cells (data not shown). One would need to harvest 1 kg of cells to produce 1 g of *Ao*Cld to perform all the planned experiments. It was, therefore, essential for this project to improve the enzyme expression and purification, which are described in section 3.1.1 and 3.1.2, respectively, to achieve a higher yield.

3.1.1 Optimisation of the enzyme expression in *E.coli* and preparative enzyme production

To optimise the enzyme production in the host organism *E.coli* BL21(DE3)pLysS with the pET28a vector carrying the gene for *Ao*Cld, four parameters were investigated that can have a significant influence on the enzyme expression levels: the IPTG and hemin concentration, the temperature after induction, and the harvest time point.

The effects of the changed conditions were quantified with activity measurements (section 2.4.3) or on SDS-PAGE (section 2.4.2). The specific activities of the new conditions, after cell lysis and without any further purification, were compared to the specific activity of the original cultivation protocol [23]. Three rounds of improvements were carried out.

Influence of the IPTG concentration on the specific activity of *Ao*Cld

In the first round, the influence of the IPTG concentration on the specific activity of the enzyme was investigated (Table 3-1). The original cultivation protocol [23] stated to induce the enzyme expression with 1 mM IPTG. If the IPTG concentration is reduced to 500 µM, the specific activity can be increased 4-fold (Table 3-1). High IPTG concentrations induce stress in the microorganism, promote the storage of the enzyme in inclusion bodies instead, and are toxic to the cells [53].

If the IPTG concentration is lowered, even more, the specific activity decreased (Table 3-1). A particular IPTG concentration is necessary to induce the complete dissociation of the lac repressor. It was, therefore, decided to use 500 µM IPTG for the induction of the enzyme expression for further optimisation.

Table 3-1. Investigation of cultivation parameters for the enzyme optimisation. Volumetric activities were measured in duplicates. An asterisk (*) marks the activity of the original cultivation protocol [23].

	Sample	Cell wet weight [g]	Volume [mL]	Activity [U mL^{-1}]	Specific Activity [U mg^{-1}]
	50 µM IPTG	0.55	0.85	380 ± 6	0.58 ± 0.01
	100 µM IPTG	0.47	0.69	845 ± 72	1.24 ± 0.11
	500 µM IPTG	0.56	1.01	3978 ± 269	7.20 ± 0.49
	1000 µM IPTG*	0.44	1.14	659 ± 7	1.71 ± 0.02
25°C	40 µg mL^{-1} hemin	0.87	1.02	3651 ± 161	4.26 ± 0.19
25°C	60 µg mL^{-1} hemin	0.56	1.44	2868 ± 203	7.35 ± 0.52
25°C	80 µg mL^{-1} hemin	0.55	0.90	1175 ± 26	1.93 ± 0.04
30°C	40 µg mL^{-1} hemin	0.65	1.27	1630 ± 129	3.19 ± 0.25
30°C	60 µg mL^{-1} hemin	0.6	1.37	1297 ± 146	2.96 ± 0.33
30°C	80 µg mL^{-1} hemin	0.64	1.11	1129 ± 111	1.95 ± 0.20

Influence of the hemin concentration and cultivation temperature on the specific activity of *Ao*Cld

In the second round, the influence of the hemin concentration and the temperature after induction were analysed simultaneously. The standard protocol [23] states to use 40 µg mL^{-1} of hemin in the cultivation media and to reduce the temperature from 37°C to 30°C after the induction with IPTG. Only hemin concentrations above 40 µg mL^{-1} were examined, as Geus and co-workers reported to us that hemin was necessary to see any enzyme production. Hemin helps to incorporate the heme cofactor into the active site of the enzyme. Furthermore, two temperatures were tested, as the reactor, where the enzyme will be produced later in a larger scale, cannot cool below 25°C.

The best result was obtained by increasing the hemin concentration to 60 µg mL^{-1} and by reducing the temperature after IPTG induction further to 25°C (Table 3-1). The temperature is an essential factor, because a lower temperature helps the proper folding of the enzyme, as the microorganism grows slower than at 37°C (the temperature optimum of *E. coli*). *E. coli* can invest more time in the enzyme production [54].

Influence of the harvest time on the specific activity of *Ao*Cld

To improve the enzyme production even further, the time for harvesting was investigated in more detail, as overexpressed protein is often stored in inclusion bodies after long cultivation times [55]. If enzymes are stored in inclusion bodies, it becomes more challenging to retain the protein, which is undesirable. The original protocol [23] stated to harvest the cell culture 16 hours after induction with IPTG. To determine a new potential harvesting time point, cells from one cell culture were harvested 3 hours, 5 hours, and 7 hours after IPTG induction.

Figure 3-1A shows that the amount of enzyme in the supernatant increases from 3 hours to 7 hours (lane 1, 3, 5). The colour of the supernatant after cell lysis becomes redder as well (Figure 3-1B). The intense red colour [56] is another indication of more *Ao*Cld present in the soluble fraction. However, the amount of enzyme in the insoluble fraction increases over time as well (Figure 3-1A, lane 2, 4, 6). At 16 hours, on the contrary, more protein appears in the cell pellet (Figure 3-1A, lane 8) than in supernatant (Figure 3-1A, lane 7). The longer *E. coli* is exposed to IPTG and has to produce *Ao*Cld, the more protein is stored in inclusion bodies, as a stress response.

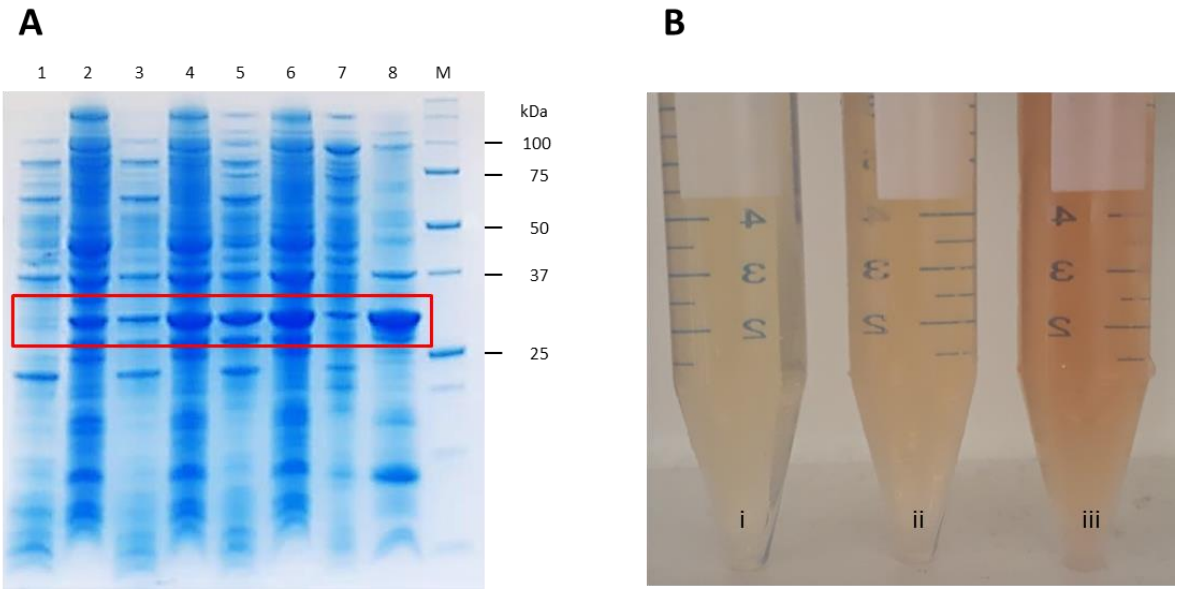

Figure 3-1. Determination of a harvest time point. A – SDS loaded with 25 µg per well after cell lysis. 1 – supernatant 3 h after induction (ind.), 2 – cell pellet 3 h after ind., 3 – supernatant 5 h after ind., 4 – cell pellet 5 h after ind., 5 – supernatant 7 h after ind., 6 – cell pellet 7 h after ind., 7 – supernatant 16 h after ind., 8 – cell pellet 16 h after ind., M stands for Precision Plus Protein™ All Blue Standards Marker by Bio-Rad. The red box marks the height of the expected *Ao*Cld monomer (28 kDa). B – the colour of the supernatant after cell lysis for 3 hours (i), 5 hours (ii), and 7 hours (iii).

Table 3-2 summarises the activity of different time points. The specific activity in the supernatant increases 8-fold from 3 hours to 7 hours after IPTG induction. Whereas the specific activity of the supernatant at 16 hours after IPTG induction is reduced by 2-fold. The SDS-PAGE shows (Figure 3-1A) that the amount of enzyme in the insoluble fraction builds up with longer cultivation times, but also the specific activity confirms this assumption (Table 3-2). It was decided to harvest the cell cultures 7 hours after induction with IPTG.

After these optimisation experiments, a new cultivation procedure was established and it was possible to increase the specific activity 6-fold with this new protocol.

Table 3-2. Determination of a harvest time point. Ind. = induction. Volumetric activities were measured in duplicates.

Sample	Cell wet weight [g]	Volume [mL]	Activity [U mL^{-1}]	Specific Activity [U mg^{-1}]
Supernatant 3 h after ind.	0.8	7	141 ± 19	1.23 ± 0.17
Pellet 3 h after ind.	0.55	3	14.5 ± 1.5	0.079 ± 0.008
Supernatant 5 h after ind.	0.82	7.8	661 ± 12	6.29 ± 0.12
Pellet 5 h after ind.	0.7	3	54.9 ± 4.6	0.24 ± 0.02
Supernatant 7 h after ind.	0.73	8	1029 ± 4	9.97 ± 0.66
Pellet 7 h after ind.	0.36	3	214 ± 22	0.18 ± 0.18
Supernatant 16.5 h after ind.	4.87	25	874 ± 87	4.49 ± 0.45

Preparative enzyme production

The cultivation of *Ao*Cld was optimised successfully. The preparative enzyme production was carried out in a 15 L fermenter. The first fermentation in LB medium yielded only 80 g of cells, which corresponds to 5.3 g L^{-1}. This small yield led to the decision to change from LB to TB medium. With TB medium the yield of cells was doubled to 12 g L^{-1}, which has been tested on a small scale beforehand. TB contains 20% more tryptone and 380% more yeast-extract than LB, which extends the growth phase of *E. coli* and produces, therefore, more recombinant protein [57]. The cells were from now on grown in TB medium, as described in section 2.2.1. In total, 500 g cells were produced, which were used for purification (section 2.3).

3.1.2 Optimisation of the enzyme purification and preparative (bulk) purification

The previously established purification method in our lab (Srour, 2018) had to be redefined for scale-up, because 500 g of cells needed to be purified (section 3.1.1). This procedure included a His-tag affinity chromatography, a desalting step, and a gel filtration step. The last step, especially, is not suitable for a large scale purification, because only small volumes and diluted protein solutions (up to 20 mg mL^{-1}) can be loaded on a gel filtration column. For large amounts, a larger column is needed which results in a very long chromatography run. Because of practical reasons, the gel filtration step was eliminated from the procedure. Therefore, another method needed to be considered to remove the primary contaminant, imidazole, after the affinity chromatography step.

Imidazole was used as the main component in the elution buffer during the His-tag purification (section 2.3.1). As imidazole is used during this step in high concentrations (500 mM), imidazole occupies the vacant side of all hemes in the enzyme solution. Imidazole binds with a high affinity of 11.5 ± 1.3 µM to the heme group (result of BEP student Pepijn Kooij), which proposes a challenge to remove the contaminant. The goal of this part of the work was to establish a new purification protocol that is suitable for scale-up and removes imidazole successfully without gel filtration.

The combination of two desalting steps, the desalting with a HiTrap column material and a PD10 desalting column (section 2.3.2), changed the spectrum of the enzyme significantly (Figure 3-2). The typical spectrum with 100% imidazole bound has a sharp Soret band at 413 nm with a high absorptivity as well as an α and β band at 562 nm and 535 nm, respectively. The α and β band – a characteristic for a 6-coordinated heme iron (III) – indicate that another ligand is bound to the heme iron. The spectrum, after the two desalting steps, has a Soret band which is blue-shifted with a decreased absorptivity and a broad Soret peak with a shoulder at 406 nm (Figure 3-2).

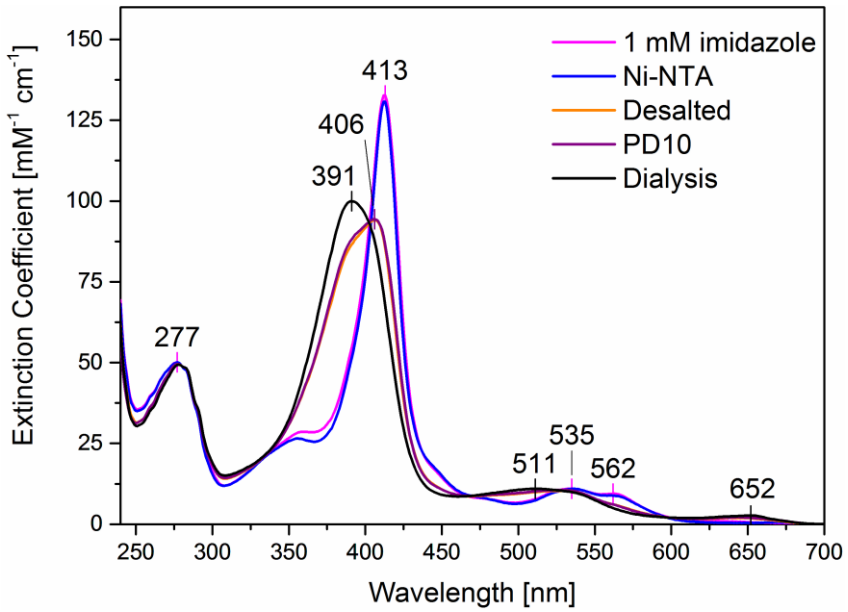

Figure 3-2. Monitoring of the imidazole removal with UV-Vis spectroscopy. UV-Vis spectra were obtained with 10 µM *Ao*Cld in 100 mM KPi buffer, pH 7, at 21°C.

EPR spectroscopy revealed that only 30% of the imidazole was removed (Figure 3-3b), as EPR still shows the typical imidazole signal ($g_{z,y,x}$ = 2.95, 2.92, 1.49). Another cleaning step had to be set up to reduce the imidazole content further.

As a further cleaning step, a dialysis was performed. With the help of the dialysis, it was possible to remove the imidazole almost completely. The Soret band in the UV-Vis spectrum shifted from 406 nm to 391 nm (Figure 3-2), similar to the reported Soret peak at 392 nm of the wildtype enzyme [37]. The EPR spectrum (Figure 3-3c) also showed that the remaining amount of imidazole was decreased to 20%.

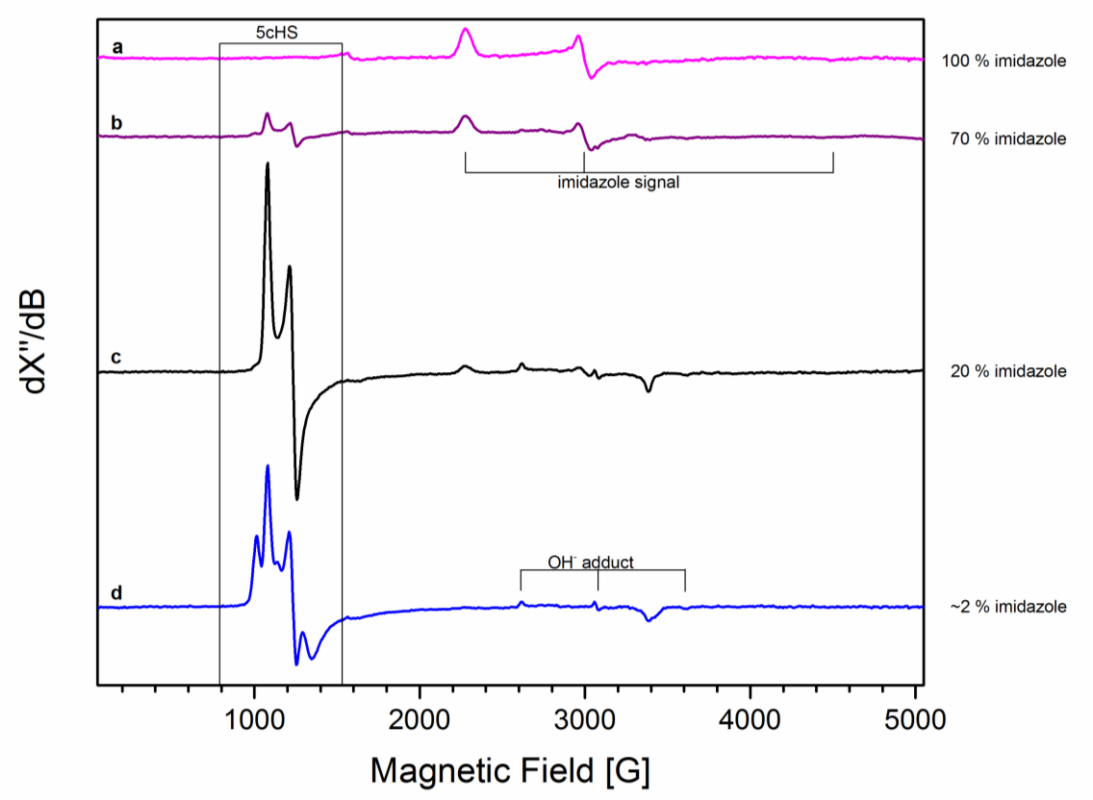

Figure 3-3. Monitoring of the imidazole removal with EPR spectroscopy. a - *Ao*Cld with 1 mM imidazole as a reference, b - *Ao*Cld after PD10 step, c - *Ao*Cld after bulk dialysis, d – *Ao*Cld dialysed to a dilution factor of 1800 in a smaller scale. The graph highlights characteristic signals of a 5-coordinate ferric high spin signal (5cHS), imidazole and OH^- adduct. EPR spectra were obtained with 75 µM *Ao*Cld in 100 mM KPi, pH 7, microwave frequency 9.4 GHz, microwave power 79 mW, modulation frequency 100 kHz, modulation amplitude 20 G, and temperature 20 K.

In a smaller scale, it was tested how much further the imidazole could be removed and if this could influence the UV-Vis and EPR spectra. The UV-Vis spectra remain the same regardless the dilution factor (Appendix C, Supp. Figure 4). Only the EPR revealed that it is possible to reduce the imidazole completely with a dilution factor of 1800 (Figure 3-3d). For practical purposes, as 600 mL of protein needed to be dialysed, only the protein from fermentation 2 (350 mL in total) was dialysed to a dilution factor of 650, as described in section 2.3.3.

The removal of imidazole was successful after three cleaning steps as it has been described above. The success of the newly established protocol has also been

followed by an SDS (Figure 3-4) and activity measurements (Table 3-3). The SDS (Figure 3-4) shows that *Ao*Cld is pure as no other protein has been co-purified.

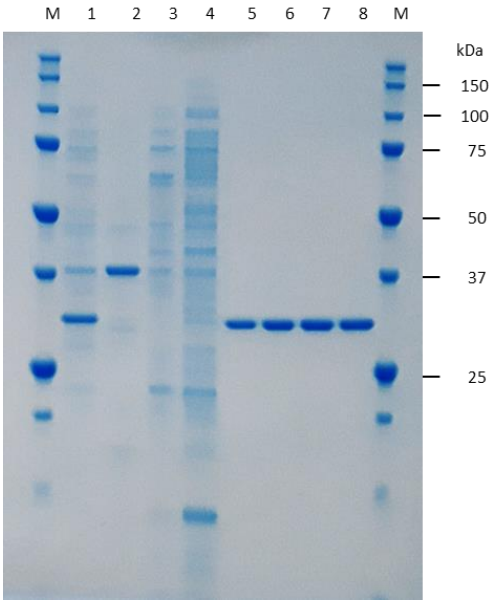

Figure 3-4. SDS-PAGE profile of *Ao*Cld purification. 10 µg protein was loaded per well. 1 – cell lysate, 2 – cell pellet, 3 – flow through of the HisTrap, 4 – washing step of the HisTrap, 5 – HisTrap purified protein, 6 – HiTrap desalted protein, 7 – PD10 purified protein, 8 – dialysed protein. M stands for Precision Plus Protein™ All Blue Standards Marker by Bio-Rad.

The purification table (Table 3-3) shows it is possible to obtain a pure enzyme. The Reinheitszahl (Rz), a commonly used parameter to characterise the purity of a heme protein, measures the ratio between the absorption of the Soret peak at 391 nm and protein peak at 280 nm, increases from 1.05 after the affinity chromatography to 2.04 after dialysis. The higher Rz is, the purer a protein can be considered [11].

Table 3-3. Purification table for the purification of *Ao*Cld produced in *E. coli*. For the complete purification table see Appendix C, Supp. Table 1.

Step	Specific Activity [U mg^{-1}]	Purification [fold]	Yield [%]	Rz [A_{391nm}/A_{280nm}]
Cell lysis	2856 ± 181	1.0	100	-
Affinity chromatography	8838 ± 138	3.1	71	1.05
HiTrap Desalting	9543 ± 345	3.3	58	1.76
PD10	9821 ± 448	3.4	49	1.80
Dialysis	8515 ± 324	3.0	40	2.04

The specific activity was improved in every step, except after the dialysis as the specific activity drops by 13% (Table 3-3). A decreased activity could be a result of the bulk dialysis, as the dialysis had to be carried out for six days to achieve a dilution factor of 650. It was, thus, impossible to achieve a dilution factor of 1800 to remove the imidazole completely.

To conclude, with the new cultivation and purification procedure, we obtained 13 mg of protein per gram of cells (Appendix C, Supp. Table 1). In total 2 g of protein was highly purified with the imidazole adduct below 20% in the protein stock solution, as shown by UV-Vis (Figure 3-2) and EPR spectroscopy (Figure 3-3c). This purified enzyme will be characterised in section 3.2 and used for the pre-steady-state experiments in section 3.3.

3.2 Characterisation of *Ao*Cld

The purified enzyme from section 3.1.2 is characterised in this section regarding spectral information, the influence of different buffers, pH values, as well as the ionic strength on the specific activity, and the kinetic properties. This characterisation is necessary, because *Ao*Cld is a highly buffer- and pH-dependent enzyme (unpublished results, 2019).

3.2.1 Spectral properties of *Ao*Cld

Spectroscopic methods are useful to characterize heme containing proteins, as seen in earlier sections. UV-Vis and EPR spectroscopy was used to characterise *Ao*Cld.

The UV-Vis spectrum of *Ao*Cld after purification exhibits a protein peak at 278 nm, a broad Soret peak at 391 nm, and charge transfer (CT) bands at 652 nm and 511 nm with a shoulder at 535 nm (Figure 3-5). This spectrum is characteristic of a 5-coordinate ferric (Fe^{3+}) heme protein [58]. The Rz (A_{391nm}/A_{280nm}) is 2.04 which confirms a successful purification (section 3.1.2). EPR (Figure 3-3c) of *Ao*Cld shows a characteristic 5-coordinated ferric high spin signal (S = 3/2) around a g-values of 6.2, which is comparable to the wildtype [37] and other pentameric Clds, like *Magnetospirillum* sp. [38]. After extensive imidazole removal, it becomes clear that a hydroxyl group binds in the vacant side to the iron instead of the imidazole (Figure 3-3c, d), which can be recognised with a low spin signal ($g_{z,y,x}$ = 2.56, 2.19, 1.87).

Sodium dithionite reduces the iron from ferric (Fe^{3+}) to ferrous (Fe^{2+}). The characteristic spectrum of reduced 6-coordinated ferrous heme protein has a red-shifted Soret peak to 433 nm with an increased absorptivity as well as an α and β band at 585 nm and 556 nm, respectively (Figure 3-5), which are an indication that a sixth ligand coordinates the heme iron [58].

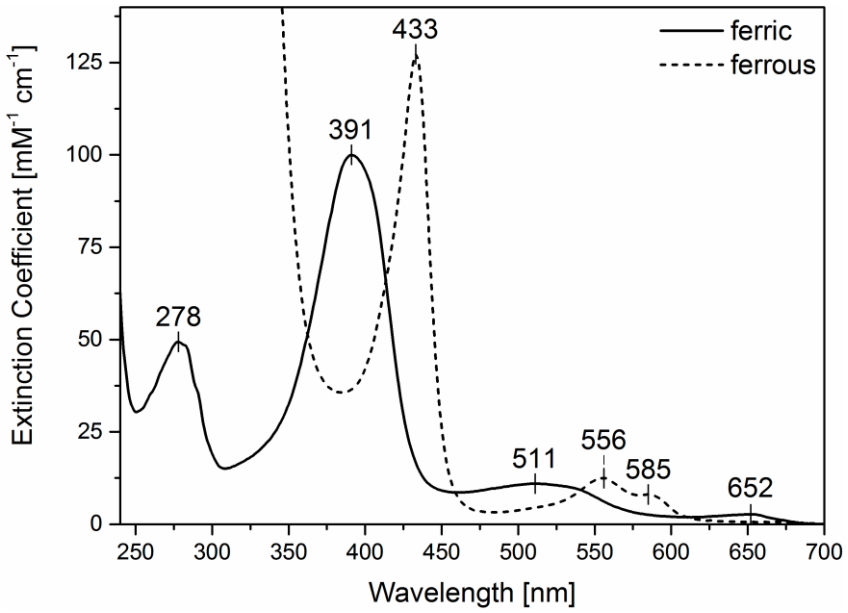

Figure 3-5. UV-Vis absorption spectra of as-prepared (solid line) and dithionite-reduced (dashed line) enzyme. 10 µM *Ao*Cld was dissolved in 100 mM KPi, pH 7. *Ao*Cld was reduced with 1 mM sodium dithionite. Spectra were taken at 21°C.

The extinction coefficients of the enzyme were calculated and are summarised in Table 3-4. The extinction coefficient of ε_{280nm} with 48.955 mM^{-1} cm^{-1} is used to determine the protein concentration for all experiments.

Table 3-4. Extinction coefficients of the ferric (Fe^{3+}) and ferrous (Fe^{2+}) form of *Ao*Cld.

Extinction coefficients of ferric *Ao*Cld		Extinction coefficients of ferrous *Ao*Cld	
ε_{278nm}	49.447 mM^{-1} cm^{-1}	ε_{400nm}	41.985 mM^{-1} cm^{-1}
ε_{280nm}	48.955 mM^{-1} cm^{-1}	ε_{433nm}	127.254 mM^{-1} cm^{-1}
ε_{391nm}	99.559 mM^{-1} cm^{-1}	ε_{556nm}	12.469 mM^{-1} cm^{-1}
ε_{400nm}	94.793 mM^{-1} cm^{-1}	ε_{585nm}	8.077 mM^{-1} cm^{-1}
ε_{511nm}	11.911 mM^{-1} cm^{-1}		
ε_{535nm}	10.366 mM^{-1} cm^{-1}		
ε_{652nm}	2.456 mM^{-1} cm^{-1}		

3.2.2 Photo-effect of *Ao*Cld

While using the stopped-flow equipment (section 2.6), it was discovered that *Ao*Cld is a light-sensitive enzyme. When the enzyme was mixed 1:1 with Milli-Q water and the spectra were measured for more than 4 ms in the cuvette, the typical ferric spectrum (Figure 3-5) changed (Figure 3-6).

The Soret band shifted to ~409 nm and decreased over time (Figure 3-6). This behaviour was unexpected and has not been reported for other Clds in literature. The experiment was repeated in another spectrophotometer to investigate this phenomenon further.

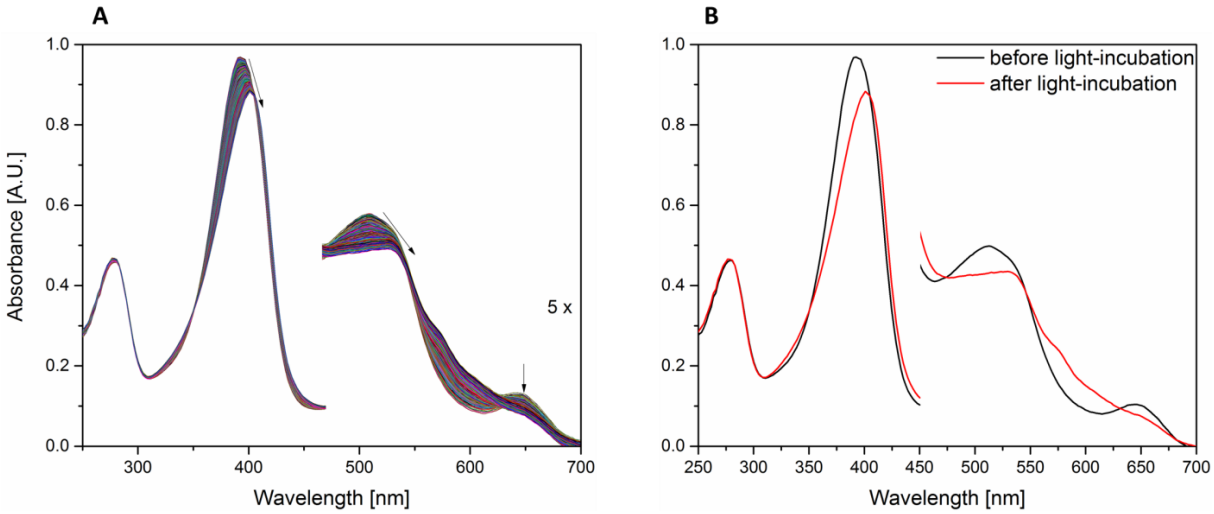

Figure 3-6. Spectral changes of *Ao*Cld mixed with Milli-Q water. 20 µM *Ao*Cld (10 µM end concentration) was mixed 1:1 with Milli-Q in a stopped-flow device at 20°C and spectra were obtained for 60 s (A). Start spectrum before light-incubation and the final spectrum after light-incubation have been illustrated for better visualization (B). Arrows indicate the direction of absorption changes. The visible regions are enlarged 5x.

The enzyme-water mixture was placed in a Cary 60 spectrophotometer from Agilent Technologies and the spectra were recorded from 200 nm to 800 nm every 30 seconds for an hour. *Ao*Cld's spectrum remains unchanged (Appendix C, Supp. Figure 5) compared to the spectra recorded on the stopped-flow machine (Figure 3-6).

Relationship between the spectrophotometer type and the photo-sensitivity of *Ao*Cld

It is hypothesised that the spectrophotometer type might play a role in this particular phenomenon. The stopped-flow is a so-called photodiode array spectrophotometer. All the light from the light source passes through the sample in the cuvette. A grating after the cuvette reflects the light to the detector (diode array). Whereas, the Cary 60 spectrophotometer is a monochromator where only light of one specific wavelength at the time passes through the sample. (The set-up of the two different spectrophotometer types is shown in Appendix B, Supp. Figure 1 and Supp. Figure 2 for a better understanding.) The exposure of the sample to light with all wavelengths instead of one single wavelength at the time could affect the protein.

To test this hypothesis, *Ao*Cld was placed in another photodiode array spectrophotometer (Hewlett Packard 8453) and the spectra were recorded from the range of 200 nm to 800 nm every 0.05 seconds. Spectral changes were induced; however, the absorptivity was not decreased as much as in the stopped-flow (data not shown). This result proves that the spectrophotometer type influences the light-sensitivity of the enzyme.

Besides the spectrophotometer type, also the intensity of the light source plays a role in how fast the enzyme is changed in the light. The Hewlett Packard 8453 has a tungsten and deuterium lamp with 25 W and the stopped-flow has a xenon arc lamp with 150 W. A photodiode array spectrophotometer with a high-intensity light source causes faster destruction of the protein. We claim that *Ao*Cld exhibits a so-called photo-effect.

Photo-effect of other heme proteins

As the stopped-flow is a commonly used machine for identifying catalytic intermediates (section 1.4), also for other Clds, it is questioned if *Ao*Cld is the only Cld and also the only heme protein exhibiting this photo-effect. Literature study revealed that the Horseradish peroxidase (HRP), a heme-dependent peroxidase, shows light-sensitive behaviour as well [59]. HRP, therefore, was used as a positive control. Cytochrome c (cyt c) from bovine heart, an electron carrier in the electron transport chain, was used as a negative control, as no literature reported the photo-effect of cyt c. Both heme proteins were dissolved in water and were incubated for a few minutes in the stopped-flow (Figure 3-7) under similar conditions as the Cld experiments to see any spectral changes. Figure 3-7 illustrates that HRP indeed is a light-sensitive enzyme and the spectra of cyt c remain unchanged during the incubation with light.

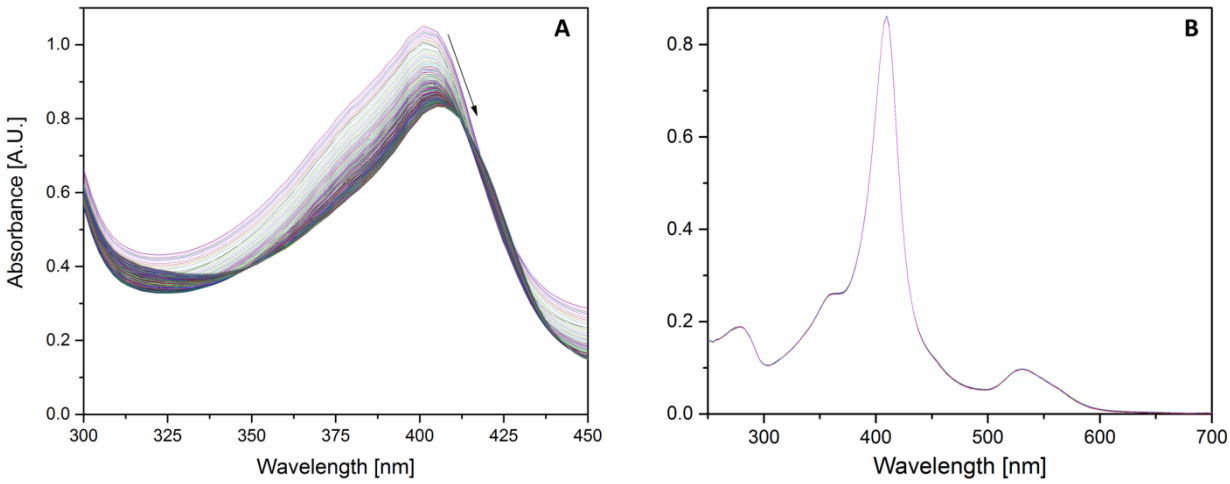

Figure 3-7. Spectral changes of Horseradish peroxidase (A) and Cytochrome c (B) mixed with Milli-Q water. 20 µM HRP and cyt c (10 µM end concentration) were mixed each 1:1 with Milli-Q in a stopped-flow device at 20°C and spectra were obtained for 60 s. Arrow indicates the direction of absorption changes.

The presumed cause for the photo-effect

These findings leave us with a question: what causes the photo-sensitivity of *Ao*Cld? At this point of this work, we cannot answer this question completely; but we found reasonable explanations. Researchers suspect that ultraviolet (UV) light induces changes in the heme moiety or amino acid residues leading to decreased enzyme activity, stability, and heme absorption [59]. Photons can ionise aromatic amino acids [60, 61] that might interact with the heme and promote heme bleaching – or in this cause photo-bleaching.

A study from Grotjohann *et al.* [62] showed that the heme dissociates from a plant catalase after it has been excited with blue light. Another study assumed that the dissociation of the heme occurs faster in acidic pH [59]. At acidic pH values, proximal and distal amino acids (mostly histidine's and arginines) are protonated, which causes the amino acids to repulse each other electrostatically leading to the release of the heme. The photo-induced release of the heme could, therefore, be the cause of a decreased activity and a diminished Soret band absorption [59].

Figure 3-6 shows that the absorption of the Soret band decreases and the CT bands disappear in *Ao*Cld upon the incubation with light. Photons might mediate the modification of the proximal histidine (His170) that leads to the displacement of the heme, as proposed by other studies [59, 61, 62]. For future work, we need to clarify which wavelength is responsible for the photo-bleaching and examine the effects of the photo-induced damages in more detail with activity measurements, EPR spectroscopy, and gel filtration to confirm the loss of the heme cofactor.

3.2.3 Influence of buffer composition, pH, and ionic strength on the enzymatic properties

The activity of Clds are known to be strongly pH-dependent. Therefore the pH and buffer dependence of *Ao*Cld was investigated. Figure 3-8 confirms the pH profile, as it has been described in our lab previously (unpublished results, 2019). The optimum pH for *Ao*Cld is 5.8. The activity drops significantly with higher or lower pH-values (Appendix C, Supp. Figure 6). Other Clds have higher activities in acidic pH as well [17, 38] because the protonated conserved distal Arg (pKa = 6.5) can facilitate the binding of the anionic substrate and might stabilise any negatively charged reaction intermediates (section 1.3) [24, 63, 64].

*Ao*Cld has the highest activity in sodium citrate buffer (100% relative activity) and citrate-phosphate buffer (89% relative activity, Figure 3-8). Those buffers show the most significant decrease between the activity of the optimum pH of 5.8 and pH 6 with 60% and 30% for sodium citrate and citrate-phosphate buffer, respectively (Figure 3-8).

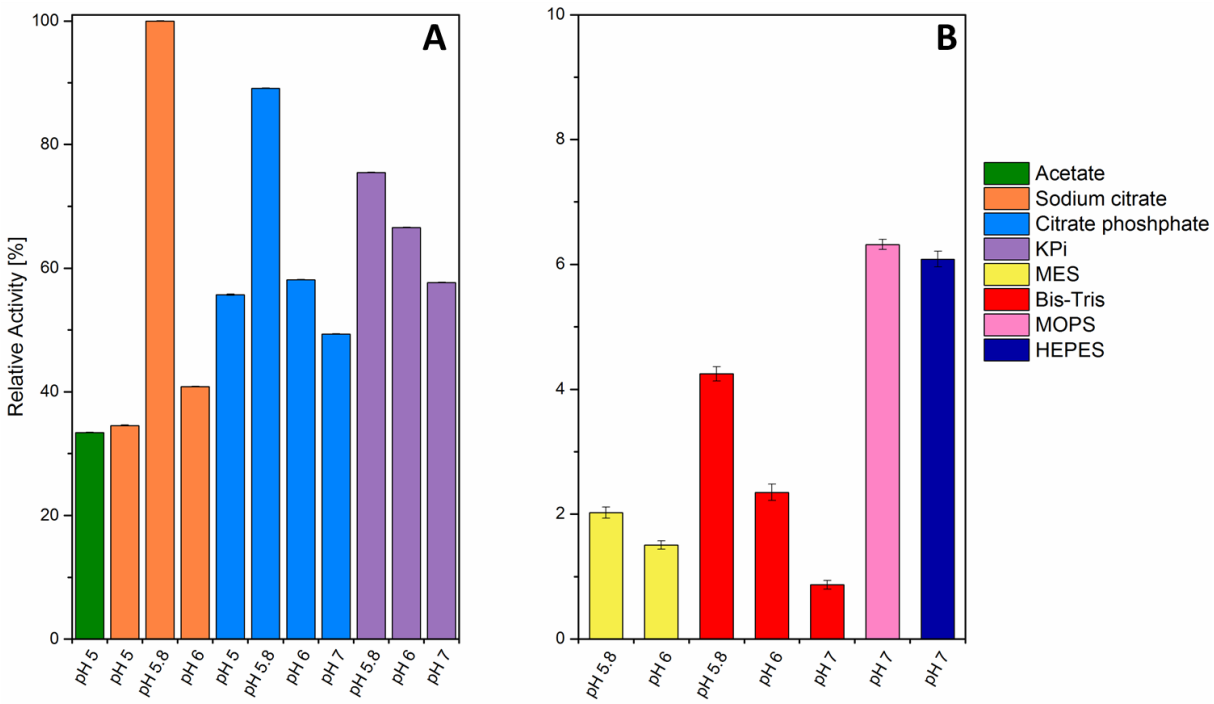

Figure 3-8. Comparison of the activity of *Ao*Cld in different buffers with different pH-values. Shown are the relative activities in acetate (green), sodium citrate (orange), citrate-phosphate (pale blue), MES (yellow), KPi (purple), Bis-Tris (red), MOPS (pink), and HEPES (blue). Specific activities were measured in 100 mM of the regarding buffer, 1 mM sodium chlorite, 125 pM to 3.8 nM *Ao*Cld, 20°C. Experiments were performed in triplicates.

*Ao*Cld possesses 30% of its activity in acetate buffer, pH 5 (Figure 3-8), and also changes colour from red to green (Appendix C, Supp. Figure 7). Acetate, which acts as a weak field ligand, was found to bind to the vacant side of the heme moiety. This binding induces a spectral change (Appendix C, Supp. Figure 8) and inhibits the activity as it blocks the binding spot for the substrate (unpublished results, 2019). If the protein is transferred rapidly back to any other buffer than acetate, the colour and the activity can be recovered (unpublished results, 2019). Crystallisation processes are ongoing to prove, not only with spectral methods or equilibrium binding experiments that acetate binds to the heme group.

Figure 3-8B shows the activity of *Ao*Cld in MES, Bis-Tris, MOPS, and HEPES dropped to ~3%. These buffers are classified as Good's buffers, which are often used for biological research because they exhibit maximum buffer capacity around the neutral pH, minimal salt effect, and high stability [65]. These buffers, which have been classified by Good *et al.* [65], are not optimal for *Ao*Cld, as the activities in these buffers are up to 60-fold lower than in other buffers tested (Figure 3-8B).

It was beyond the scope of this project to investigate this behaviour more thoroughly. It is, however, hypothesised that components of those buffers might block the access to the active site or even bind to the active site; therefore, ClO_2^- cannot reach the heme group. It might also be a possibility that components of the buffers bind further

away from the active site, which could cause conformational changes and the protein could lose the ability to catalyse the conversion of ClO_2^- to Cl^- and O_2. More experiments need to be performed to validate this hypothesis (chapter 5).

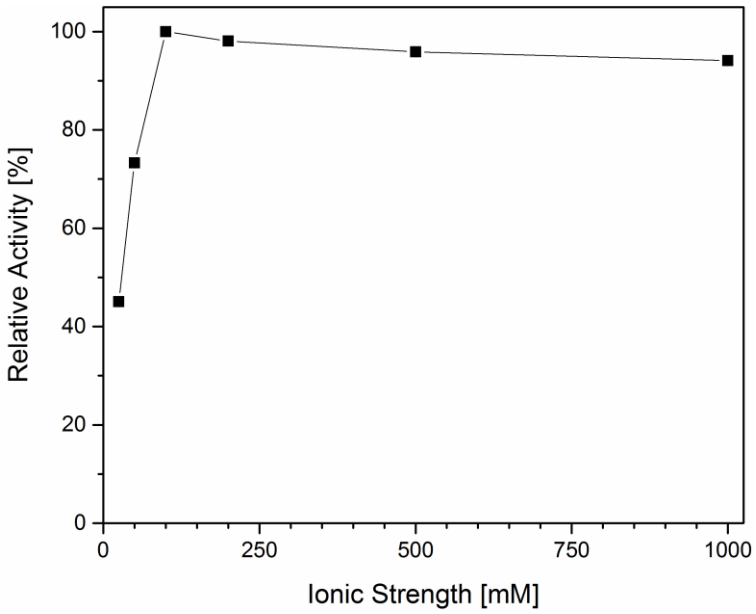

Figure 3-9. Effect of the ionic strength of KPi on the activity of *Ao*Cld. Specific activities were measured in 25 mM, 50 mM, 100 mM, 250 mM, 500 mM, and 1 M KPi buffer, pH 7, 1 mM sodium chlorite, 135 pM *Ao*Cld, 20°C. Experiments were performed in triplicates.

According to Figure 3-8, a KPi buffer (60% rel. activity) was chosen to study the (pre-)steady-state kinetics at pH 7. The influence of the ionic strength on the activity of the chosen KPi buffer was tested. A 100 mM KPi buffer resulted in the highest activity (Figure 3-9), which will be used for the rest of this work.

3.2.4 Kinetic properties of *Ao*Cld

Before exploring the pre-steady-state kinetics (section 3.3), the steady-state kinetic parameters needed to be determined. The activity was, therefore, measured with different substrate concentrations. The results of these activity measurements were fitted with Origin (Pro 2015) according to the Michaelis-Menten equation (Figure 3-10).

*Ao*Cld has an affinity (K_m) towards sodium chlorite of 276 ± 18 µM and a maximum activity (v_{max}) of 10.5 (± 0.2)·10^3 U mg^{-1} (Figure 3-10, Table 3-5). The determined K_m lies in the average range of 200 µM to 300 µM, as it has been described for other Clds, like *Dechloromonas aromatica* and *Ideonella dechloratans* (Table 3-5). The v_{max}, on the other hand, is 5x higher than the reported v_{max} of the wildtype

(2200 U mg^{-1}) [16] and the first recombinant produced *Ao*Cld by Geus *et al.* [23], which might be related that the cultivation and purification of *Ao*Cld was optimised for this work, as previously described (section 3.1). Temperature, IPTG concentration, and time point for harvest increased the amount of soluble protein, which is more active.

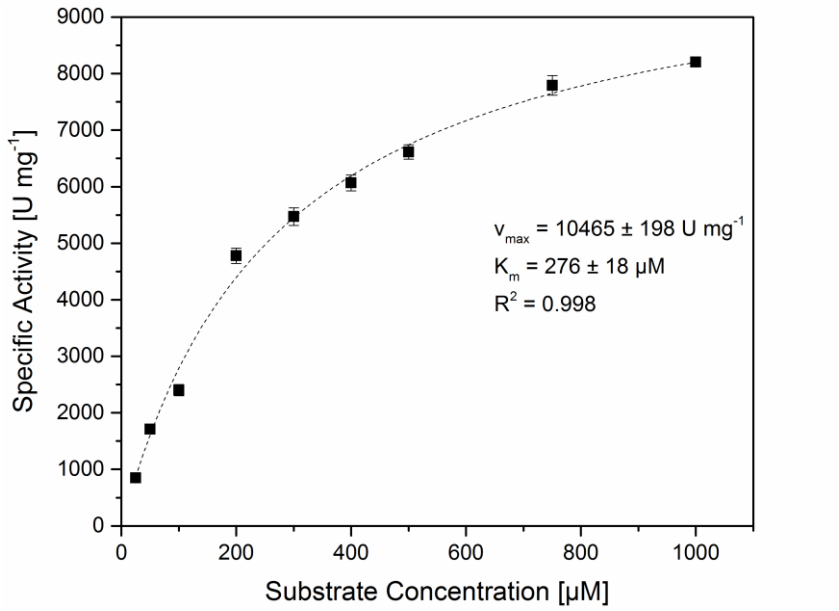

Figure 3-10. Steady-state kinetics of *Ao*Cld. Specific activities were measured in 100 mM KPi, pH 7, 25 µM to 1 mM sodium chlorite, 132 pM *Ao*Cld, 20°C. Experiments were performed in triplicates. The dotted line represents the fitted curve with Origin (Pro 2015) to the Michaelis-Menten equation.

With v_{max} and K_m, the other kinetic parameters were calculated (Table 3-5). *Ao*Cld can convert $5.2 \cdot 10^3$ ClO_2^- molecules per second to Cl^- and O_2 (k_{cat}). The turnover number k_{cat} of *Ao*Cld differs from other Clds; it is lower than the k_{cat} of *Da*Cld and *Magnetospirillum* sp. (Table 3-5), but higher than the k_{cat} of *Id*Cld and *Nd*Cld (Table 3-5).

Table 3-5. Comparison of the kinetic parameters of different Cld.

species	pH	K_m [µM]	k_{cat} [s^{-1}]	turnover time [µs]	k_{cat}/K_m [M^{-1} s^{-1}]	reference
*Ao*Cld	7	276	$5.2 \cdot 10^3$	191	$1.9 \cdot 10^7$	This work
*Da*Cld	6.8	215	$7.5 \cdot 10^3$	133	$3.5 \cdot 10^7$	[17]
*Id*Cld	7	260	$1.8 \cdot 10^3$	555	$6.9 \cdot 10^6$	[18]
Magnetospirillum sp.	6.9	1280	$12 \cdot 10^3$	83	$9.6 \cdot 10^6$	[38]
*Nd*Cld	7	69	43	$23 \cdot 10^3$	$6.2 \cdot 10^5$	[14]

The reciprocal of k_{cat} defines the time in which the disproportion of a single substrate molecule under v_{max} conditions is completed. The turnover time of *Ao*Cld is 190 µs, meaning it takes only $0.19 \cdot 10^{-3}$ seconds to convert one molecule of ClO_2^- to one molecule Cl^- and one molecule of O_2. *Ao*Cld, like any other Cld [17, 18, 38], is a fast enzyme. Since this reaction is so fast, no catalytic intermediates can be investigated with conventional methods. Hence, the reaction of *Ao*Cld with ClO_2^- has to be studied with pre-steady-state methods, as described in section 1.4.

3.3 Study of the enzyme reaction mechanism

This work aimed to investigate the reaction mechanism of *Ao*Cld with its natural substrate ClO_2^-. For this purpose, *Ao*Cld has been produced in substantial amounts (section 3.1) and has been characterised (section 3.2) to design pre-steady-state experiments to unravel the secret how *Ao*Cld can convert ClO_2^- into Cl^- and O_2. To identify any catalytic intermediates during this reaction, it is necessary to know the distinct spectral properties of these catalytic intermediates. *Ao*Cld is, therefore, first investigated with a model substrate (peracetic acid), which has been used in the past to chemically modify enzymes and induce the formation of Compound I and Compound II [26, 29, 50]. The characteristic spectra of *Ao*Cld reacted with PAA were assigned to Compound I and Compound II. These spectra lay the foundation, which will be used for the experiments with chlorite to explore any putative reaction intermediates and to propose a preliminary reaction mechanism.

3.3.1 Spectroscopic investigation of putative catalytic intermediates with the model substrate peracetic acid

Peracetic acid (PAA) is an organic peroxide, which has been used to study the formation of Compound I (Cpd I) and Compound II (Cpd II) in peroxidases [50], but also in other chlorite dismutases (Cld) [26, 29]. The formation and subsequent decay of these compounds can be followed spectroscopically (UV-Vis and EPR), because they exhibit distinct spectral features. This section will describe these distinct properties of the catalytic intermediates.

Continuous flow experiments of PAA with *Ao*Cld

The Nanosecond spectrophotometer (Nanospec) was used to mix *Ao*Cld with various PAA concentrations rapidly. After the rapid 1:1 mixing, 1900 spectra per experiment are recorded to observe the reaction (section 2.5.1). Figure 3-11 shows exemplarily a few spectra of the reaction between 350 µM *Ao*Cld and 1 mM PAA.

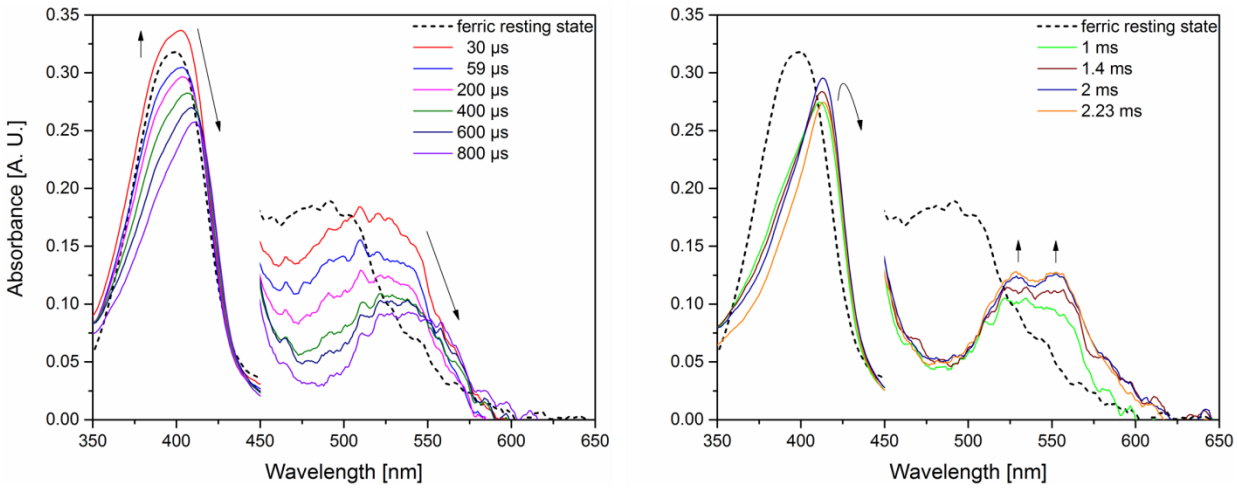

Figure 3-11. Rapid mixing of PAA and *Ao*Cld. 350 µM *Ao*Cld and 1 mM PAA, both dissolved in 100 mM KPi, pH 7, were rapidly mixed with a flow rate of 7 mL min^{-1}. Spectra were obtained with the Nanospec for 2.5 ms at 29°C. The reaction occurs so fast that the standard ferric resting state cannot be observed, but it is illustrated as a reference. Arrows indicate the direction of absorption changes. The visible region has been enlarged 5x.

*Ao*Cld and PAA rapidly reacted to form an unknown species with a maximum absorption of the Soret peak at 403 nm. The formation of this unknown species from the ferric resting state occurred so fast that the transition happened within the dead time (4 µs) of the Nanospec (The spectrum of the ferric *Ao*Cld is illustrated in Figure 3-11 as a reference, but cannot be observed during the reaction). Furthermore, the spectrum shows CT bands with a significantly broad peak around 525 nm compared with the spectrum of the ferric resting state enzyme (Figure 3-11).

The absorptivity of the new spectrum decreased by 30% after 30 µs and exhibited a new Soret peak at 410 nm. The decrease in absorptivity (hypochromicity) stopped at 800 µs, before the spectrum started to red-shift to 414 nm with prominent α and β bands at 550 nm and 530 nm, respectively (Figure 3-11). The absorption at 414 nm increased until 2 ms after the mixing. *Ao*Cld bleached out shortly after this, as the spectra at 414 nm lost the intensity of the heme band (Figure 3-11).

The raw data, as illustrated in Figure 3-11, were implemented into the modelling software KinTek to calculate the rate constants of the decaying unknown intermediates. We analysed the experimental data using singular value decomposition (SVD) to extract information about distinct species with a specific spectral property out of the data (section 2.5.3) [51]. The SVD analysis showed that during the reaction with PAA, three distinct species play a role (Figure 3-12).

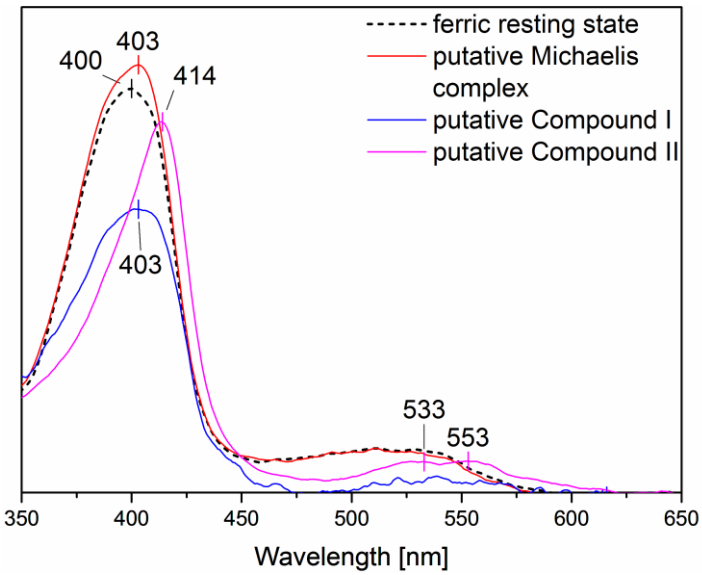

Figure 3-12. Reconstructed spectra of the catalytic intermediates of the reaction of PAA and *Ao*Cld. Arbitrary representation of the result of the SVD analysis through KinTek. The ferric resting state spectrum is illustrated as a reference.

The first unknown species exhibits a broad Soret band with a shoulder at 403 nm, which has a higher absorptivity than *Ao*Cld in its resting state (Figure 3-12). The CT bands between native *Ao*Cld and the first intermediate are the same (Figure 3-12). This species is assumed to be the Michaelis complex (Fe(III)-OOAc) of *Ao*Cld and PAA. The rate of the formation of the first species occurs too rapid that the experimental data lack spectral information for this step. Therefore, a rate constant cannot be calculated.

Nonetheless, KinTek computed the rate of the conversion of the Michaelis complex to the second intermediate. The rate constant was calculated for each experiment (various PAA concentrations) individually (Table 3-6). The conversion of the first species was fitted linearly (Figure 3-13A) with $k_2 = 2.15 \cdot 10^3\ s^{-1}$. The rate k_2 is independent of the substrate concentration at low PAA concentration, but decreases at higher PAA concentrations (Table 3-6). PAA might influence the enzyme, as an acetate leaving group could be involved in the reaction and it has been shown that acetate has a negative effect on the activity of *Ao*Cld (section 3.2.3).

The second species shows characteristics with a decreased Soret peak with a shoulder at 403 nm and a decreased absorptivity for the CT bands (Figure 3-12), which is prominent for a Cpd I, as it has been described for horseradish peroxidase [66]. The formation of Cpd I can be described with the rate constant of the decay of the Michaelis complex ($2.15 \cdot 10^3\ s^{-1}$). The conversion of Cpd I to the third unknown intermediate was calculated individually (Table 3-6) and fitted with a hyperbola with a rate constant $k_3 = 15.13 \cdot 10^3\ s^{-1}$ (Figure 3-13B). Cpd I does not accumulate during the reaction with PAA because the decomposition of Cpd I is faster than its formation (Table 3-6).

Table 3-6. Calculated rate constants for the reaction of PAA and *Ao*Cld. k_2 – formation rate of Compound I and k_3 – formation rate of Compound II. An asterisk (*) marks the outlier data point, which has not been included in the fit.

PAA concentration [mM]	k_2 [$\cdot 10^3$ s^{-1}]	k_3 [$\cdot 10^3$ s^{-1}]
1	2.12	2.25
5	1.89	5.55
10	1.93	8.03
20	1.81	9.41
30	*2.53**	11.37
40	1.05	13.18

The spectrum of the third species is red-shifted with a narrow Soret band at 414 nm and prominent α and β bands at 550 nm and 530 nm, respectively (Figure 3-12), which might resemble Cpd II [66]. An example spectrum for Cpd I and Cpd II from horseradish peroxidase is illustrated in Appendix B, Supp. Figure 3 for comparison. Since *Ao*Cld was chemically modified with PAA, *Ao*Cld cannot return to the ferric resting state (Fe^{3+}), despite the claim of other studies [29] that Cld does return to its ferric resting state. Therefore, it is degrading, which was observed in a decreasing absorption of the Soret band at 414 nm (Figure 3-11). This degradation was insignificant in these experiments because the Nanospec can observe the reaction only for 2.5 ms. A complete degradation, however, could be followed in an Agilent spectrophotometer (Appendix C, Supp. Figure 9), where the hypochromicity at 414 nm was followed for 30 min.

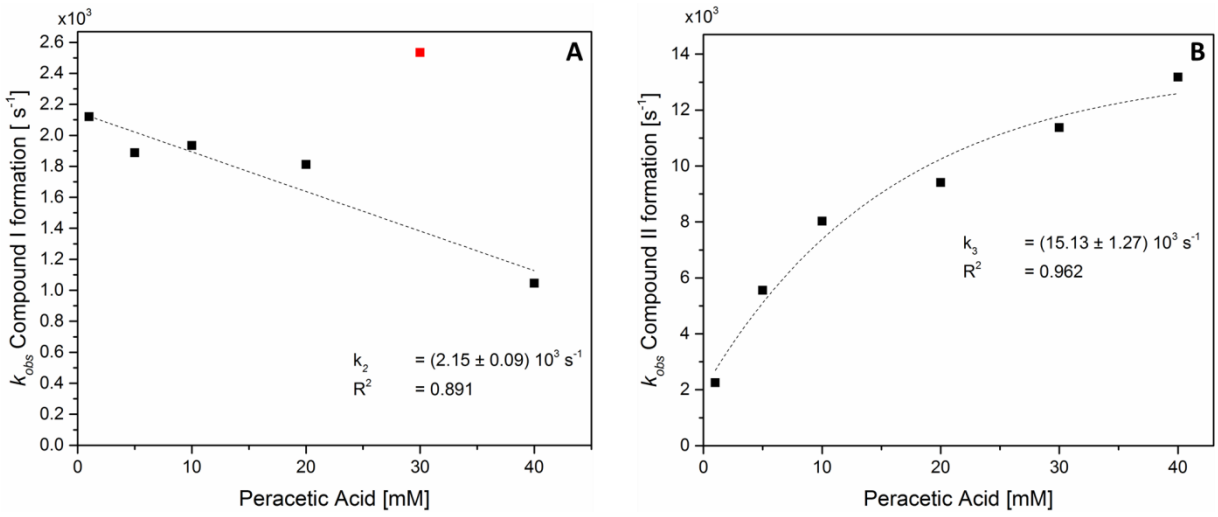

Figure 3-13. Fitting of the rate constants for the formation of Compound I (A) and for the formation of Compound II (B). 350 µM *Ao*Cld were rapidly mixed with 1, 5, 10, 20, 30, and 40 mM PAA. A – rate constants for the formation of Compound I (k_2) were fitted linearly. The outlier is masked red, which has not been included in the fit. B – rate constants for the formation of Compound II (k_3) were fitted with a hyperbola.

These experiments confirmed the theory that PAA induces the formation of a Cpd I and Cpd II in an enzyme (Figure 3-12). The spectral properties of Cpd I and Cpd II of *Ao*Cld are comparable to other catalytic intermediates of peroxidases or Clds (Table 3-7). Cpd II was hereby the last stage before *Ao*Cld degraded (Appendix C, Supp. Figure 9).

Table 3-7. Comparison of the spectral properties of the catalytic intermediates of *Ao*Cld, other Clds, and HRP. ND = not determinable.

Species	pH	Soret	CT1	β	α	CT2	reference
*Ao*Cld Cpd I	7	403	ND	ND	ND	ND	This work
*Ao*Cld Cpd II	7	414	-	533	553	-	This work
*Da*Cld Cpd I	6	395	600	525	550	-	[29]
*Da*Cld Cpd II	6	412	-	525	555	-	
*C*Cld Cpd I	5	406	650	-	-	-	[22]
*C*Cld Cpd II	5	418	-	528	551	-	
HRP Cpd I	10	400	646			583	[66]
HRP Cpd II	10	420		525	551		

Rapid freeze-quench experiments of PAA and *Ao*Cld

Specific EPR signals have been reported for Cpd I and Cpd II (Figure 1-10) [67, 68]. Therefore, PAA and *Ao*Cld were rapidly mixed 1:1 in the microsecond freeze-hyperquenching device (MHQ) under the same conditions as in the Nanospec (section 2.5.1) and the reaction was quenched at different time points.

To choose time points at which the reaction between *Ao*Cld and PAA had to be quenched, a PAA concentration had to be determined. Table 3-6 shows that Cpd I does not accumulate, as $k_3 > k_2$. The best option to capture Cpd I was to choose a low PAA concentration (1 mM), as the difference between k_3 and k_2 is the smallest. As the Nanospec experiments were conducted at 29°C, the rate constants from the reaction with 1 mM PAA (Table 3-6) had to be transformed to rate constants at 9°C (operation temperature of the MHQ) with the Eyring equation (Appendix A, equation 2). At 9°C, the Cpd I will be formed in 443 s^{-1} and the Cpd II will be formed in 449 s^{-1}. With these rate constants, the kinetic traces could be reconstructed and the EPR could be prepared.

Figure 3-14 summarises the results of the EPR measurements of the MHQ prepared samples (for all time point see Appendix C, Supp. Figure 10). The EPR showed at 97 µs a different high spin signal compared to the ferric resting state with a decreased intensity and an anisotropic radical signal appears with a $g_\perp$ value of 2.005 (Figure 3-14B). The high spin ferric signal disappeared with time (Figure 3-14C, D), while the intensity of the radical signal increased over time (Figure 3-14D). To identify

this radical signal, the magnetic field was scanned from 3160 G to 3560 G to improve the resolution of the signal (Figure 3-15).

The radical showed a typical amino acid-based radical with $g_{\perp}$ value of 2.005, which could either be a tryptophan- or tyrosine-based radical (Figure 1-10B) [50, 67]. A protein-based radical is likely, because two tryptophan as well as one tyrosine are close to the active site of *Ao*Cld. To determine the correct origin of the radical signal, mutagenesis experiments need to be performed to see if the radical still can be formed if the regarding amino acid was mutated.

It is assumed that the radical signal at 800 µs and 16 ms (Figure 3-14C, D) are different. The radical at 800 µs could be an amino acid radical coupled to the Compound I, as this EPR spectrum exhibits other signals at g_z = 3.37 and g_y = 2.24, which are close to the g-values reported in literature for the Compound I of the ascorbate peroxidase [68]. The radical at 16 ms could be an amino acid radical associated with Compound II [50]. However, at this point this is an assumption. To verify this hypothesis, more time points of the reaction need to be constructed, which will need to be more extensively measured, regarding different microwave frequencies and different microwave powers (saturation plots) to define the radicals closer.

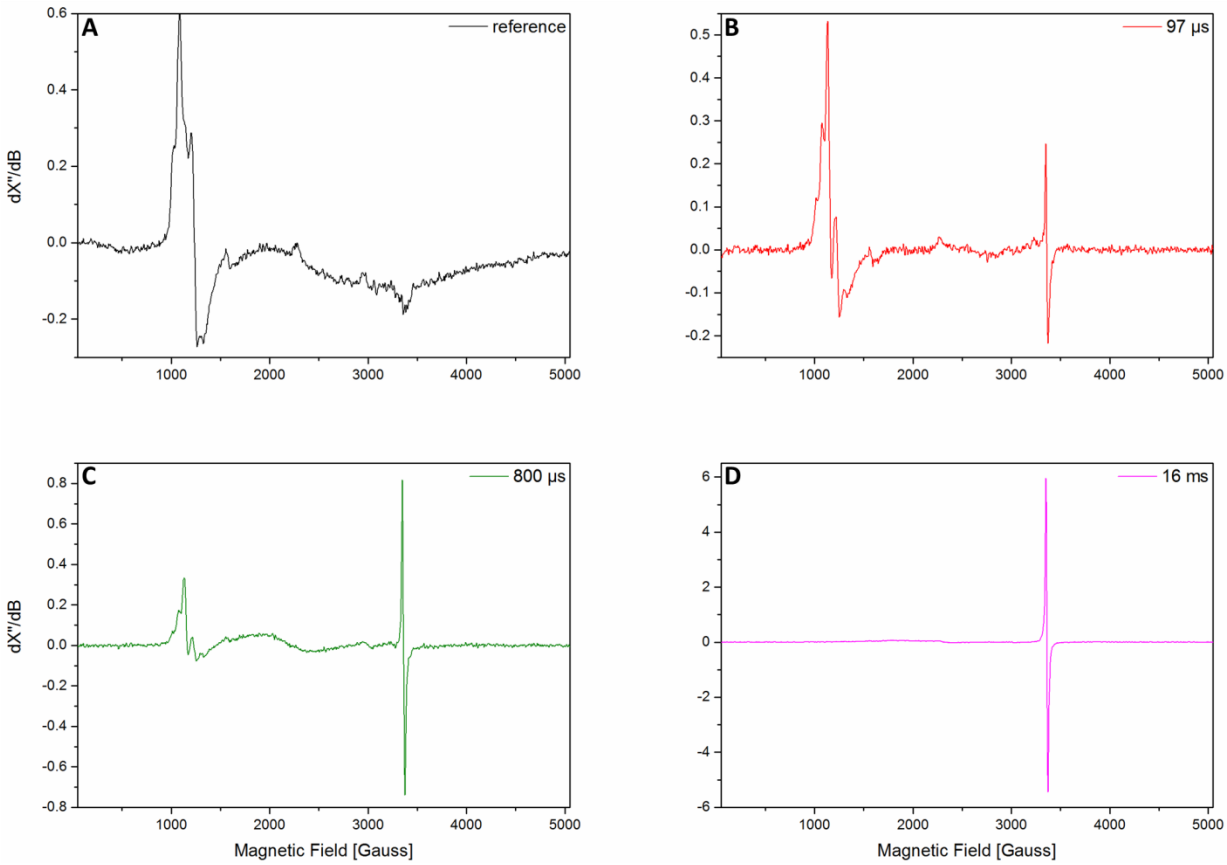

Figure 3-14. EPR spectra of the MHQ prepared samples with PAA and *Ao*Cld. 1.5 mM PAA and 500 µM *Ao*Cld, both dissolved in 100 mM KPi, pH 7, were mixed at 9°C and frozen rapidly. A – 500 µM *Ao*Cld and 100 mM KPi buffer, pH 7, have been mixed for a reference spectrum. The reaction between PAA and *Ao*Cld was quenched 97 µs (B), 800 µs (C), and 16 ms (D) after mixing. EPR spectra were obtained with microwave frequency 9.4 GHz, microwave power 20 mW, modulation frequency 100 kHz, modulation amplitude 10 G, and temperature 20 K.

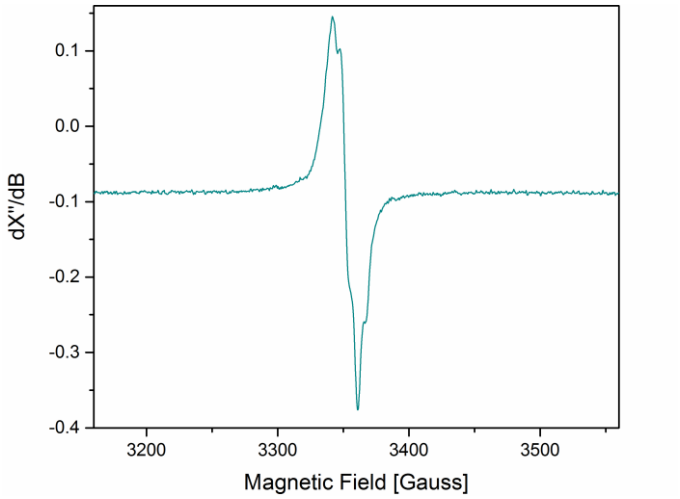

Figure 3-15. Close-up EPR spectra of the MHQ prepared sample with PAA and *Ao*Cld 16 ms after mixing. 1.5 mM PAA and 500 µM *Ao*Cld, both dissolved in 100 mM KPi, pH 7, were mixed at 9°C and frozen rapidly 16 ms after mixing. EPR spectrum was obtained with microwave frequency 9.4 GHz, microwave power 0.2 mW, modulation frequency 100 kHz, modulation amplitude 2 G, and temperature 20 K. 4x average.

To conclude, PAA has the ability to chemically modify enzymes in such a way that they are forming Compound I and Compound II. We propose a preliminary reaction mechanism (Figure 3-16) that PAA binds to Fe^{3+} of *Ao*Cld to form a Michaelis complex. The binding step occurs fast and the O-O bond of PAA is cleaved heterolytically to yield Compound I and an acetate anion with a rate constant of $2.15 \cdot 10^3$ s^{-1}. The cation radical migrates from the porphyrin ring to the acetate anion or an nearby amino acid to form an acetate or amino acid radical and Compound II with a first-order rate constant of $15.13 \cdot 10^3$ s^{-1}. After the formation of Compound II, *Ao*Cld bleaches out as it cannot return to its ferric resting state as Cpd II is a dead-end for the enzyme.

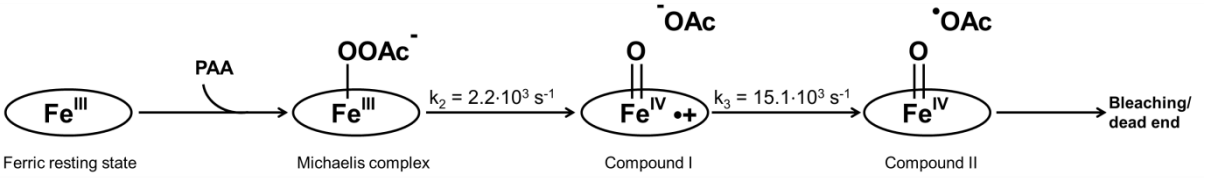

Figure 3-16. Proposed reaction scheme between peracetic acid and *Ao*Cld.

Other research groups have proposed reaction mechanisms of Cld with PAA as well. It becomes challenging to compare them, as either they are performed with other chemicals, like hypochlorite [22]; or the reactions with PAA are performed at different pH-values [29]. The study of Lee *et al*. used PAA at pH 7 to chemically modify *Da*Cld [26]. The overall reaction they observed was ten times slower (20 ms) than our observation (2 ms). Furthermore, the formation of Compound II in *Ao*Cld is two orders of magnitude faster than the Compound II formation in *Da*Cld (170 s^{-1}). It was expected that these two Cld behave similarly as they have similar structural and kinetic properties, but it is too early to draw any conclusion why they react differently.

However, additional information is needed to prove the presence of Cpd I and Cpd II. The claim should be supported by other methods as well, for instance Resonance Raman spectroscopy (chapter 5). EPR provides at this stage inconclusive results, as not enough time points have been extensively measured. For future experiments, more EPR measurements need to be performed and sequential mixing studies should be conducted. For example, Lee *et al*. and Mayfield *et al*. showed that Cpd I and Cpd II can be transformed back to the ferric state if these were mixed with two or one equivalents of ascorbate, respectively [26, 29].

3.3.2 Spectroscopic investigation of putative catalytic intermediates with the natural substrate chlorite

After investigating the catalytic intermediates from the reaction with PAA, it is scientific relevant to examine, if the reaction with ClO_2^- follows the same order. However, it is challenging to observe the reaction with the natural substrate, as the reaction will be completed within 200 µs (section 3.2.4). Therefore, not many researchers have studied the reaction with ClO_2^- in detail, also due to the limitation of equipment. The stopped-flow is the most common pre-steady-state device, but cannot measure below 1 ms (section 1.4.2).

In this section, the results of the reaction of ClO_2^- and *Ao*Cld, which was followed spectroscopically (UV-Vis and EPR), are presented and the distinct spectral features will be matched with the results of the reaction with PAA.

Continuous flow experiments with chlorite and *Ao*Cld

*Ao*Cld is rapidly mixed with various sodium chlorite concentrations in the Nanospec. Figure 3-17 shows exemplarily a few spectra of the reaction between 330 µM *Ao*Cld and 50 mM sodium chlorite. *Ao*Cld and ClO_2^- rapidly reacted to form an unknown species with a narrow Soret peak at 408 nm. The formation of this unknown species from the ferric resting state occurred within the dead time of the Nanospec (The spectrum of the ferric *Ao*Cld is illustrated in Figure 3-17 as a reference, but cannot be observed during the reaction). Furthermore, the spectrum showed different CT bands with a decreased absorptivity compared with the spectrum of the ferric resting state (Figure 3-17).

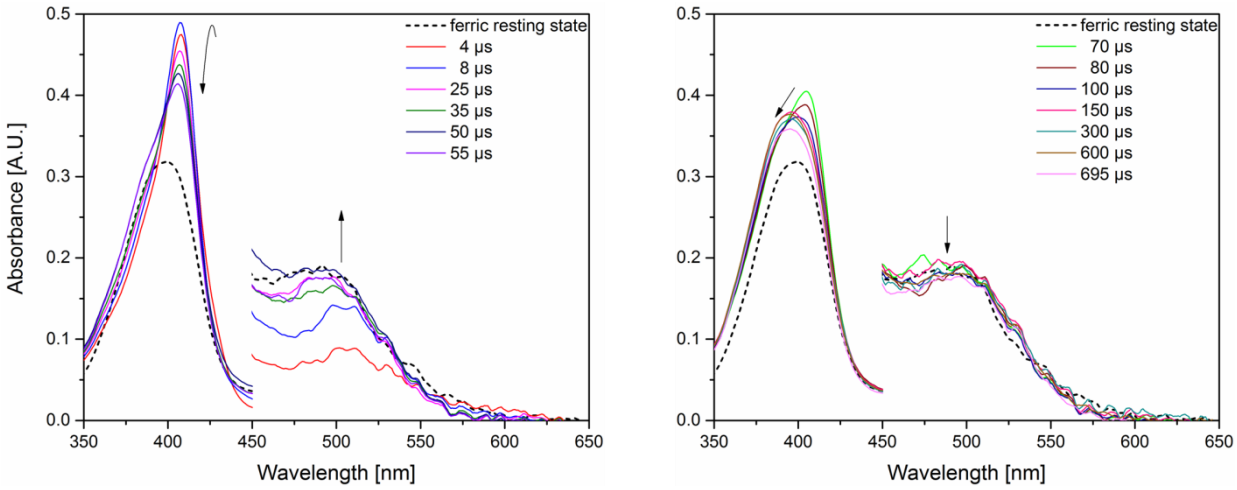

Figure 3-17. Rapid mixing of sodium chlorite and *Ao*Cld. 330 µM *Ao*Cld and 50 mM sodium chlorite, both dissolved in 100 mM KPi, pH 7, were rapidly mixed with a flow rate of 20 mL min^{-1}. Spectra were obtained with the Nanospec for 700 µs at 29°C. The reaction occurs so fast that the standard ferric resting state cannot be observed, but it is illustrated as a reference. Arrows indicate the direction of absorption changes. The visible region is enlarged 5x.

The unknown species reached its absorption maximum at 408 nm, 8 µs after mixing before it decreased and started to blue-shift (Figure 3-17). The decrease in absorptivity stopped after 100 µs at 395 nm (Figure 3-17). As the Nanospec can only measure until 700 µs after mixing, it can be assumed that the spectrum returns to its ferric starting position as all recorded spectra exhibited a higher absorptivity than the ferric spectrum. The measurement of *Ao*Cld with ClO_2^- in a conventional spectrophotometer showed that the enzyme returned to its standard Fe^{3+} resting state spectrum (Appendix C, Supp. Figure 5).

The CT band around 500 nm had already returned to the shape of the standard spectrum (Figure 3-17). The reaction might be in steady-state at 700 µs, as it would take 30 ms to complete 150 turnovers (150 equivalents of ClO_2^- react with *Ao*Cld and one turnover takes 200 µs), which might explain why the spectrum had not returned completely to the ferric form yet.

The raw data, as illustrated in Figure 3-17, were analysed using KinTek which calculated the rate constant of the decaying unknown intermediate. The SVD analysis showed that during the reaction with chlorite two distinct species play a role (Figure 3-18).

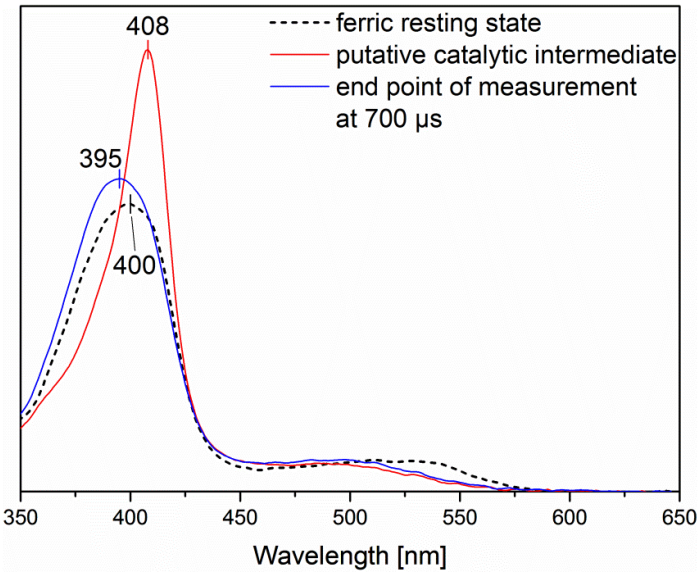

Figure 3-18. Reconstructed spectra of the catalytic intermediates of the reaction of sodium chlorite and *Ao*Cld. Arbitrary representation of the result of the SVD analysis through KinTek. The ferric resting state spectrum is illustrated as a reference.

The unknown species exhibits a sharp Soret band at 408 nm, which has a higher absorptivity than the *Ao*Cld in its resting state (Figure 3-18). If this spectrum is compared to the spectra of the reaction with PAA (Figure 3-12), neither Cpd I nor Cpd II exhibit a Soret band at 408 nm. It is, therefore, challenging to attribute the

spectrum of the catalytic intermediate of the chlorite reaction to either Cpd I or Cpd II at the moment.

Since there is no spectral information available for the formation of this intermediate, but for its decay, KinTek calculated an apparent rate constant k_{obs} for every chlorite experiment (Table 3-8).

Table 3-8. Calculated rate constants for the reaction of sodium chlorite and *Ao*Cld.

Chlorite concentration [mM]	k_{obs} [$\cdot 10^4$ s^{-1}]
10	4.57
20	3.40
30	2.69
40	2.15
50	1.87

The rate constants for the conversion of the catalytic intermediate was fitted single exponentially with k = $51 \cdot 10^3$ s^{-1} (Figure 3-19). The rate of the conversion from the putative catalytic intermediate to the ferric resting state slows down with higher chlorite concentrations. The formation of this intermediate might be faster than its breaking down and a high substrate concentration pushes the equilibrium towards its formation. The intermediate, therefore, accumulates and needs more time for its conversion.

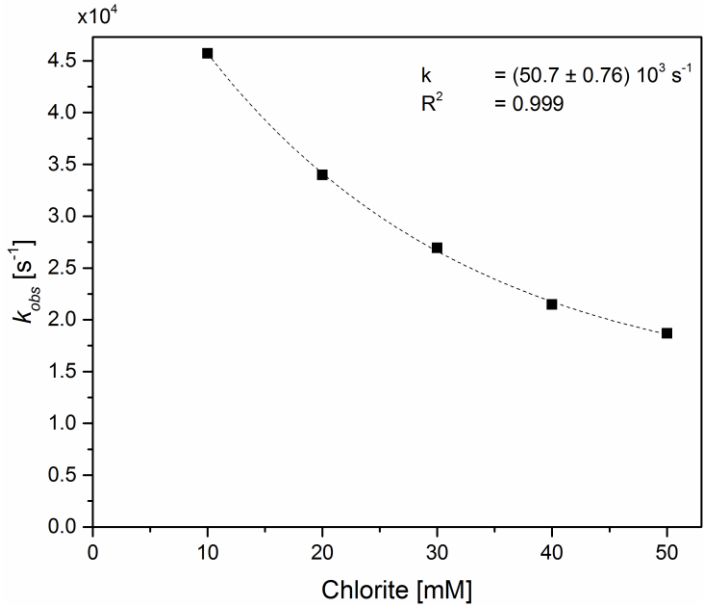

Figure 3-19. Fitting of the rate constant for the decay of the putative catalytic intermediate. 330 µM *Ao*Cld were rapidly mixed with 10, 20, 30, 40, and 50 mM sodium chlorite. Rate constant for the decay of the putative catalytic intermediate (k) was fitted with a single exponent.

Rapid freeze-quench experiments with chlorite and *Ao*Cld

The Nanospec experiments showed that *Ao*Cld reacts with ClO_2^- and immediately forms a catalytic intermediate whose identity is not entirely verified yet. Therefore, chlorite and *Ao*Cld needed to be mixed rapidly in the MHQ.

Table 3-8 shows that the putative intermediate converts at higher chlorite concentrations slower back to the ferric resting state as the intermediate might accumulate. Therefore, it could be possible to capture any intermediate before the reaction is in steady-state. The rate constant from the reaction of 50 mM chlorite had to be transformed to a rate constant at 9°C with the Eyring equation (Appendix A, equation 2). At 9°C, the putative intermediate would convert in $4.3 \cdot 10^3$ s^{-1}. With this rate constant, the kinetic traces could be reconstructed and EPR samples could be prepared. Figure 3-20 summarises the results of the EPR measurements (for all time points see Appendix C, Supp. Figure 11).

The EPR showed at 97 µs a more axial high spin signal (S = 5/2) with increased intensity compared with the ferric resting state (Figure 3-20B). A different high spin signal indicates that the environment of the iron has changed, but its oxidation state (Fe^{3+}) remains unchanged. The new high spin signal might be an evidence for the rebinding of a reaction intermediate (either hypochlorite or chlorine monoxide) to the iron. The Fe(III)-peroxyhypochlorite complex has an oxidation state of 3+ (Figure 1-3), which strengthens this hypothesis.

A radical signal appeared at 97 µs with a $g_{y,x}$ = 2.025, 2.0098 (Figure 3-20B). This radical signal was unusually broad with clear partially resolved hyperfine structures and is accompanied by a low spin signal with $g_{y,x}$ = 2.32378, 2.005. In the reaction with PAA, however, such a radical signal was not observed (Figure 3-14). It is assumed that this could be Cpd I associated with an amino acid-based radical (called Compound I*). Mayfield *et al*. have measured a similar low spin signal with $g_{\perp}$ = 2.0055 and a radical signal, which they attributed as Compound I* [29]. Schaffner *et al*. also claim that Cpd I* might play a role during the reaction mechanism [22]. More EPR measurements need to be conducted to resolve the region of the radical in more detail, to prove the claim of an amino acid-based radical associated with Cpd I (chapter 5).

The rhombic high spin ferric signal (S = 3/2) was restored with time (Figure 3-20D), but looks different than the ferric resting state high spin signal (Figure 3-20A). The reaction between *Ao*Cld and chlorite at 200 ms could be in steady-state and multiple spectra are overlaying that form an altered signal which is slightly different from the resting high spin signal. This supports the Nanospec data (Figure 3-17) where 80% of the 1900 UV-Vis spectra are close to the ferric resting state spectrum, but exhibit a Soret band at 395 nm with a higher absorptivity. This different spectrum could be the result of multiple spectra that are overlaying.

The radical signal changed over time (Figure 3-20D) to a similar radical signal as in the reaction with PAA (Figure 3-14D). The radical shows as well a typical amino acid-based radical with a $g_{\perp}$ value of 2.005, which could either be a tryptophan- or tyrosine-based radical [50, 67]. This indicates that a Cpd II might be formed during the reaction. The reconstructed spectra (Figure 3-18) from the Nanospec data illustrated that the catalytic intermediate exhibits a sharp and narrow Soret band at 408 nm, which did not match the reconstructed spectra from the PAA reaction (Figure 3-12). However, the shape of this sharp and narrow Soret peak resembles the form of the spectrum of Cpd II from PAA at 414 nm. The PAA could induce our discovered acetate effect (section 3.2.3) which might lead to the different wavelengths of the Soret peak. Therefore, new model substrates should be tested to validate this claim (chapter 5).

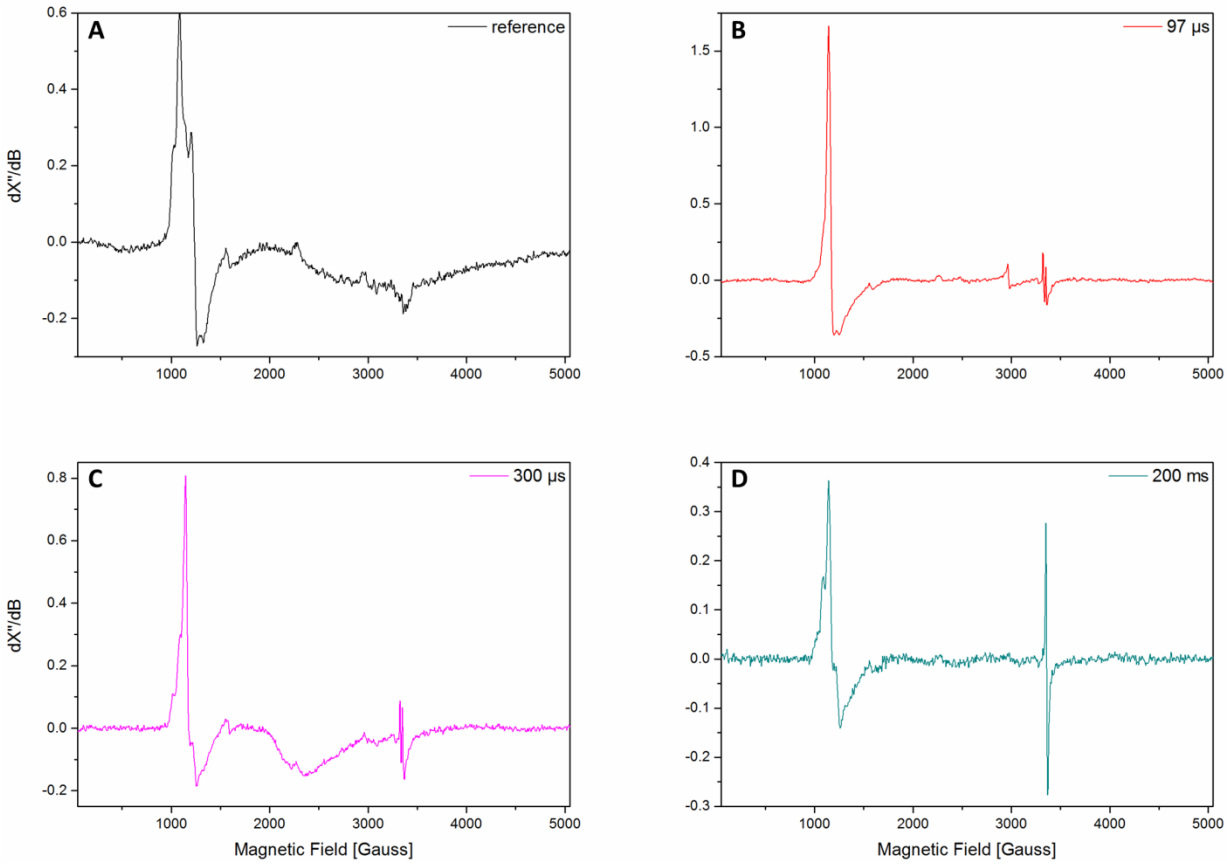

Figure 3-20. EPR spectra of the MHQ prepared samples with sodium chlorite and *Ao*Cld. 75 mM sodium chlorite and 500 µM *Ao*Cld, both dissolved in 100 mM KPi, pH 7, were mixed at 9°C and frozen rapidly. A – 500 µM *Ao*Cld and 100 mM KPi buffer, pH 7, have been mixed for a reference spectrum. The reaction between sodium chlorite and *Ao*Cld was quenched 97 µs (B), 300 µs (C), and 200 ms (D) after mixing. EPR spectra were obtained with microwave frequency 9.4 GHz, microwave power 20 mW, modulation frequency 100 kHz, modulation amplitude 10 G, and temperature 20 K.

The results of the EPR showed that two different transient radical species arise during the reaction with the natural substrate. One of these radical signals in the

microsecond timescale (Figure 3-20B, C) was not found in the reaction with PAA (Figure 3-14). The EPR spectrum delivers clues that this could be an amino acid-based radical associated with Cpd I (Compound I*) similar to the EPR spectrum of HRP [68] and cytochrome c peroxidase [69] with a proven CPD I*. However, the Nanospec data did not show any spectra that can be attributed to Cpd I, as this intermediate might not accumulate enough during the reaction. It is assumed that Compound I is relatively instable at neutral pH and converts fast to Compound II [70]. Therefore, many more experiments need to be designed to resolve these spectra fully.

To conclude, the analysis of EPR and Nanospec data led to the discovery of catalytic intermediates for the real reaction between *Ao*Cld and ClO_2^-. We can, therefore, propose a preliminary reaction mechanism (Figure 3-21), which is similar to mechanism III in section 1.3 (Figure 1-3).

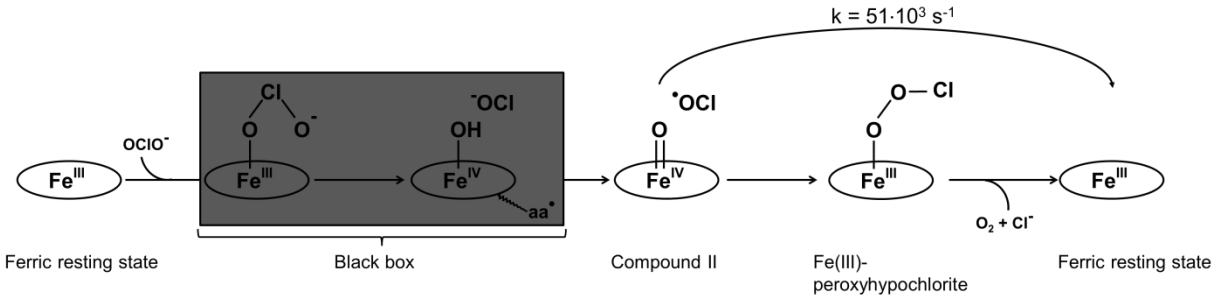

Figure 3-21. Scheme for a proposed reaction mechanism between chlorite and *Ao*Cld. The Michaelis complex and Compound I* are surrounded by a black box as the data are limited to fully assign them.

*Ao*Cld reacts immediately with chlorite to form a Michaelis complex and the O-Cl bond is cleaved heterolytically to yield a Compound I*, which is coupled to a nearby tryptophan- or tyrosine-based radical, and hypochlorite ($^-$OCl) as a reaction product. These formations occur so rapidly that they might lie in the dead time (4 µs) of the Nanospec. The transient Compound I*, however, can be seen in the EPR (Figure 3-20B). Therefore, more studies need to be conducted to prove that Cpd I* is involved in the real reaction. This could be approached by slowing down the reaction with different reaction conditions (e.g. different buffer composition). This approach could be precarious, as these major changes could severely influence the kinetic mechanism.

Furthermore, Compound I* converts to Compound II by an electron transfer step between hypochlorite and the porphyrin ring. Compound II has been detected by the Nanospec and the EPR. Chlorine monoxide rebinds to the iron (Fe(III)-peroxyhypochlorite), therefore, Compound II converts with $51 \cdot 10^3$ s^{-1} to the ferric resting state to repeat the catalytic cycle (Figure 3-21).

4 Conclusion

This work aimed to study the conversion of ClO_2^- to Cl^- and O_2 by the chlorite dismutase of *Azospira oryzae* (*Ao*Cld) in more detail. It was essential for this endeavour to prepare substantial amounts of pure *Ao*Cld. A cultivation optimisation achieved a ~6-fold increase in the specific activity of *Ao*Cld. To facilitate this improvement, it was necessary to halve the IPTG concentration and the cultivation time, as well as to decrease the temperature after the induction with IPTG.

It proved to be surprisingly difficult to remove the contaminant imidazole after affinity chromatography, which was accomplished by introducing three cleaning steps: HiTrap method, PD10, and dialysis as salt removal. These methods reduced the imidazole content by 80%. Improving the cultivation and the purification procedure led to a yield of 13 mg protein per g of cells. Overall, 2 g of pure *Ao*Cld was produced for this work.

After the production of the enzyme, *Ao*Cld was characterised to describe spectral properties and the activity in different conditions. We found that *Ao*Cld is a highly buffer- and pH-dependent enzyme, which loses its activity almost entirely in all tested Good's buffer. This peculiar behaviour has to be described in more detail in future research.

Furthermore, we discovered that *Ao*Cld is a photo-sensitive enzyme when it is exposed to a Xenon arc lamp of 150 W. This phenomenon is new for researchers working on Cld, but also on other heme enzymes. Previously published results on stopped-flow experiments with Clds have to be critical re-evaluated. This finding will hopefully stimulate researchers all over the world to pursue further investigations regarding a photo-induced bleaching of the heme group.

Once the foundation for the pre-steady-state studies has been laid, the reactions of *Ao*Cld with a model substrate and its natural substrate were investigated regarding putative catalytic intermediates. The UV-Vis and EPR studies with PAA showed that *Ao*Cld forms a Michaelis complex with PAA which is subsequently cleaved heterolytically to yield Compound I and an acetate leaving group. The cation radical migrates from the heme moiety to form a protein-based radical and Compound II. However, Compound II is a dead end for the enzyme and it cannot return to its ferric resting state.

The studies with chlorite proved for the first time that a putative Compound I* and a Compound II are involved in the reaction mechanism. Due to the limited data, we cannot clearly assign a Compound I*. However, the EPR data hint that a Compound I* might play a role during the reaction mechanism. More experiments need to be conducted to finalise such a hypothesis. These discoveries will pave the way to explore the disproportionation mechanism of Clds further.

5 Recommendations

The most challenging part during the preparative enzyme production was the removal of imidazole, which tightly binds to the heme group of *Ao*Cld. Imidazole is a commonly used eluent during affinity chromatography. To circumvent the imidazole contamination, either *Ao*Cld could be recloned with another Tag, for instance, a Strep-Tag; or *Ao*Cld could be eluted with thrombin instead of imidazole during HisTrap. Since cloning can be cumbersome, a protein called thrombin can cleave the His-tag and therefore elute the protein from the nickel column without using imidazole. A thrombin cleavage site is already incorporated in the plasmid. However, this approach needs to be tested because thrombin cleaves near arginine sites [71]. *Ao*Cld possesses an Arg residue close to its active site (Arg183), which might play a crucial role during catalysis. A third option could be to try ionic exchange chromatography again, which have been conducted but failed during my master thesis. A bulk dialysis could be avoided, which mostly saves resources and time for the experimenter.

During the characterisation of *Ao*Cld, we were left with two main questions, which could not be solved in the framework of a master thesis. Firstly, the particular behaviour of *Ao*Cld in Good's buffers. The activity of *Ao*Cld in those buffers is negligible. Another study about the Cld from *Magnetospirillum* sp. also reported that their enzyme is barely active in these buffers [38]. In-depth kinetic studies need to be performed to examine if another ionic strength or more substrate would help to improve the activity in these buffers. Furthermore, I was thinking to conduct docking studies to find out if a component of these Good's buffers could block the entrance to the active site or could bind to the enzyme changing its confirmation.

Secondly, the unique phenomenon that *Ao*Cld starts to degrade upon incubation in a high energy light source needs to be researched in more detail. The so-called photo-effect needs to be recreated outside the stopped-flow chamber. The treated sample can then be analysed with EPR and gel filtration to examine if the heme group is released because photons can ionise amino acid residues. Furthermore, the enzymatic activity has to be tested to confirm the study from Neves-Petersen *et al*. that the photo-inactivation also causes activity loss [59]. A photo-incubated sample could be used for crystallisation to visually prove a heme release.

Moreover, the main goal of this master thesis was to find any possible catalytic intermediates of *Ao*Cld with the reaction of ClO_2^- and study the enzyme mechanism in more detail. Indeed, we were able to find putative intermediates, but the obtained data are somewhat limited to make a precise conclusion about the mechanism. It is, therefore, advisable for further research to create more time points in the MHQ and extensively measure them with EPR. This means to make saturation power plots for the different radical species as well as to vary the microwave power and frequency to

resolve the different spin states closer. The main goal should be to find out if the amino acid-based radical is coupled to the metal centre or not (e.g. by lowering the temperature used during EPR measurements). If yes, then a special Compound I (Compound I*) is involved; if no, we could attribute the catalytic intermediate as a Compound II. Furthermore, the nearby tyrosine and tryptophan need to be mutated (for example to a phenylalanine) to attribute the radical signal to either one of these amino acids.

Another technique could be used to assign the catalytic intermediates more clearly, as frozen samples have already been prepared. Resonance Raman spectroscopy can be used to study how the frequency of the iron differs during the reaction. The frequency changes differently if a porphyrin cation radical or a ferryl species is formed.

My last suggestion to investigate the reaction mechanism closer is to find another model substrate than peracetic acid (PAA). After PAA has bound to the heme group, it is cleaved heterolytically forming an acetate leaving group. We found that acetate can bind to the iron as well, changing spectral properties, decreasing the activity and colouring *Ao*Cld green (unpublished results, 2019). It was also challenging to superimpose UV-Vis spectra of PAA and chlorite, which makes the identification of putative intermediates more difficult. However, experiments with the Cld from *Dechloromonas aromatica* and hydrogen peroxide failed [29]. A compound III-like intermediate is immediately formed in their reaction, but DuBois *et al.* can only use the stopped-flow. We, on the other hand, have access to equipment that can measure in the microsecond range. Therefore, this reaction should be recreated in our lab to find out if hydrogen peroxidase can be used to force *Ao*Cld into a Compound I and a Compound II form. Furthermore, we could recreate the experiments of Schaffner *et al.* who have used hypochlorite to initiate Cpd I and Cpd II formation [22]. Maybe the spectra of Cpd I and Cpd II match better with the spectra from the reaction with chlorite and, therefore, hypochlorite could be a better model substrate.

After all these experiments, we should have gained more insight into the enzymatic mechanism of *Ao*Cld. These insights are useful to prepare *Ao*Cld for applicative purposes. A convenient application for *Ao*Cld would be the bioremediation of chlorite contaminated water. Therefore, my successors should study the maximum tolerable levels of chlorite and chloride for the enzyme. It is currently suspected that we face substrate or product inhibition during the reaction. If so, *Ao*Cld could be engineered to improve this tolerance against chlorite and chloride. It is also worth noticing that ClO_2^- could be entirely converted by *Magnetospirillum* sp. at 4°C [38]. We usually measure at 20°C. To investigate this further, a new activity assay needs to be implemented, as we measure the oxygen production with the Clark electrode, but chlorite degradation can be followed spectroscopically at 260 nm. In the far future, *Ao*Cld can be immobilised for wastewater treatment plants.

Acknowledgement

I want to express my gratitude to many people who have helped me to realise this project. First of all, I would like to thank Peter-Leon for introducing me to the world of pre-steady-state kinetics. He has helped me to understand the complex theory behind fast kinetics and has guided me to critical view scientific literature. Thank you for all the EPR measurements which we could not have done it without you. Of course, we prepared many more samples for you to keep us in good memory. Moreover, I am very thankful for all the long Friday afternoon meetings where we tried to unravel all the mysteries we have encountered throughout the way.

Many (uncountable) credits go to the two people who have shaped my daily life in the past months. Durga, my lab partner in crime, has had my back all the time. We went through all ups and downs together, shared many laughs, and motivated each other. I will never forget our late night harvesting sessions where we danced with our cells to Bollywood music. Together we were able to tackle everything. If it was not for her, I would still be purifying my enzyme, because this project's scope was beyond the time of a master thesis and I could not have done it without her. I will deeply miss you by my side.

Furthermore, I would like to appreciate the time Marc has invested in this project and me/us. He showed us all the equipment, helped us in producing our enzyme, discovered with us the photo-effect, and was there for us when we needed him. Because of Marc, we were able to perform last-minute MHQ experiments as we were running out of time. I really enjoyed our long and intense whiteboard sessions where we went crazy about theories on how the enzyme could work (I am just saying: "what if…"). Sorry for making you late all the time, but I think you accomplished your mission in turning me into a troubleshooting queen. (P.S. thank you for being the sweetest person the past two weeks who helped me during my writing-up struggles.)

I was also able to get to know the world of teaching, because I co-supervised Pepijn (BEP). Your curiosity in the project and general research has helped me to engage even more with the project than I thought I already had. Thank you for that little push.

My gratitude also goes to my office mates, Andrada, Tania, and Sabry who shared valuable tips, laughs, hugs, and most important food with me in these last stressful weeks. I would also like to thank the whole BOC team who have made my working experience enjoyable and fun. Last but not least, I thank my family and friends (here and in Germany) who motivated me, cheered me up, took my mind off work, and pushed me to work harder.

References

[1] G.S. Moore, E.J. Calabrese, Toxicological effects of chlorite in the mouse, *Environ Health Perspect 46*, 1982, 31-37.

[2] R.W. Gullick, M.W. Lechevallier, T.S. Barhorst, Occurrence of perchlorate in drinking water sources, *J Am Water Works Assoc. 93*, 2001, 66-77.

[3] J.D. Coates, L.A. Achenbach, Microbial perchlorate reduction: rocket-fueled metabolism, *Nat Rev Microbiol 2*, 2004, 569-580.

[4] World Health Organisation (WHO), Chlorite and Chlorate in Drinking-water. Background document for development of WHO Guidelines for Drinking-water Quality., 2005.

[5] World Health Organisation (WHO), Chlorine Dioxide, Chlorite and Chlorate in Drinking-water. Background document for development of WHO Guidelines for Drinking-water Quality., 2016.

[6] J. Wolff, Perchlorate and the Thyroid Gland, *Pharmacol Rev 50*, 1998, 89-106.

[7] G.E. Ericksen, The Chilean nitrate deposits, *Am Sci 71*, 1983, 366-374.

[8] W.E. Motzer, Perchlorate: Problems, Detection, and Solutions, *Environ Forensics 2*, 2001, 301-311.

[9] T. McDonough, Bleaching Agents, Pulp and Paper, *Kirk-Othmer Encyclopedia of Chemical Technology*, 2000, Weinheim: WILEY-VCH Verlag GmbH & Co. KGaA.

[10] G.B. Rikken, A.G.M. Kroon, C.G. van Ginkel, Transformation of (per)chlorate into chloride by a newly isolated bacterium: reduction and dismutation, *Appl Microbiol and Biotechnol 45*, 1996, 420-426.

[11] S. Hofbauer, I. Schaffner, P.G. Furtmuller, C. Obinger, Chlorite dismutases - a heme enzyme family for use in bioremediation and generation of molecular oxygen, *Biotechnol J 9*, 2014, 461-473.

[12] A.W. Rutherford, Photosystem II, the water-splitting enzyme, *Trends Biochem Sci 14*, 1989, 227-232.

[13] F. Maixner, M. Wagner, S. Lücker, E. Pelletier, S. Schmitz-Esser, K. Hace, E. Spieck, R. Konrat, D. Le Paslier, H. Daims, Environmental genomics reveals a functional chlorite dismutase in the nitrite-oxidizing bacterium '*Candidatus Nitrospira defluvii*', *Environ Microbiol 10*, 2008, 3043-3056.

[14] J. Kostan, B. Sjöblom, F. Maixner, G. Mlynek, P.G. Furtmüller, C. Obinger, M. Wagner, H. Daims, K. Djinović-Carugo, Structural and functional characterisation of the chlorite dismutase from the nitrite-oxidizing bacterium "*Candidatus Nitrospira defluvii*": Identification of a catalytically important amino acid residue, *J Struct Biol 172*, 2010, 331-342.

[15] B. Goblirsch, R.C. Kurker, B.R. Streit, C.M. Wilmot, J.L. DuBois, Chlorite Dismutases, DyPs, and EfeB: 3 Microbial Heme Enzyme Families Comprise the CDE Structural Superfamily, *J Mol Biol 408*, 2011, 379-398.

[16] G. Ginkel, G. B Rikken, A. G. M. Kroon, S. Kengen, Purification and characterization of chlorite dismutase: A novel oxygen-generating enzyme, *Arch Microbiol 166*, 1996, 321-326.

[17] B.R. Streit, J.L. DuBois, Chemical and Steady-State Kinetic Analyses of a Heterologously Expressed Heme Dependent Chlorite Dismutase, *Biochemistry 47*, 2008, 5271-5280.

[18] K. Stenklo, H. Danielsson Thorell, H. Bergius, R. Aasa, T. Nilsson, Chlorite dismutase from *Ideonella dechloratans*, *J Biol Inorg Chem 6*, 2001, 601-607.

[19] G. Mlynek, B. Sjöblom, J. Kostan, S. Füreder, F. Maixner, K. Gysel, P.G. Furtmüller, C. Obinger, M. Wagner, H. Daims, K. Djinović-Carugo, Unexpected Diversity of Chlorite Dismutases: a Catalytically Efficient Dimeric Enzyme from *Nitrobacter winogradskyi*, *J Bacteriol 193*, 2011, 2408-2417.

[20] B.R. Goblirsch, B.R. Streit, J.L. DuBois, C.M. Wilmot, Structural features promoting dioxygen production by *Dechloromonas aromatic*a chlorite dismutase, *J Biol Inorg Chem 15*, 2010, 879-888.

[21] D.C. de Geus, E.A. Thomassen, P.L. Hagedoorn, N.S. Pannu, E. van Duijn, J.P. Abrahams, Crystal structure of chlorite dismutase, a detoxifying enzyme producing molecular oxygen, *J Mol Biol 387*, 2009, 192-206.

[22] I. Schaffner, G. Mlynek, N. Flego, D. Puhringer, J. Libiseller-Egger, L. Coates, S. Hofbauer, M. Bellei, P.G. Furtmuller, G. Battistuzzi, G. Smulevich, K. Djinovic-Carugo, C. Obinger, Molecular Mechanism of Enzymatic Chlorite Detoxification: Insights from Structural and Kinetic Studies, *ACS Catal 7*, 2017, 7962-7976.

[23] D.C. de Geus, E.A. Thomassen, C.L. van der Feltz, J.P. Abrahams, Cloning, expression, purification, crystallization and preliminary X-ray diffraction analysis of chlorite dismutase: a detoxifying enzyme producing molecular oxygen, *Acta Crystallogr Sect F Struct Biol Cryst Commun 64*, 2008, 730-732.

[24] B. Blanc, J.A. Mayfield, C.A. McDonald, G.S. Lukat-Rodgers, K.R. Rodgers, J.L. DuBois, Understanding how the distal environment directs reactivity in chlorite dismutase: spectroscopy and reactivity of Arg183 mutants, *Biochemistry 51*, 2012, 1895-1910.

[25] S. Hofbauer, C. Gruber, K.F. Pirker, A. Sundermann, I. Schaffner, C. Jakopitsch, C. Oostenbrink, P.G. Furtmuller, C. Obinger, Transiently produced hypochlorite is responsible for the irreversible inhibition of chlorite dismutase, *Biochemistry 53*, 2014, 3145-3157.

[26] A.Q. Lee, B.R. Streit, M.J. Zdilla, M.M. Abu-Omar, J.L. DuBois, Mechanism of and exquisite selectivity for O–O bond formation by the heme-dependent chlorite dismutase, *Proc Natl Acad Sci U.S.A. 105*, 2008, 15654-15659.

[27] M.J. Zdilla, A.Q. Lee, M.M. Abu-Omar, Concerted Dismutation of Chlorite Ion: Water-Soluble Iron-Porphyrins As First Generation Model Complexes for Chlorite Dismutase, *Inorg Chem 48*, 2009, 2260-2268.

[28] J.L. DuBois, S. Ojha, Production of dioxygen in the dark: dismutases of oxyanions, *Met Ions Life Sci 15*, 2015, 45-87.

[29] J.A. Mayfield, B. Blanc, K.R. Rodgers, G.S. Lukat-Rodgers, J.L. DuBois, Peroxidase-type reactions suggest a heterolytic/nucleophilic O-O joining mechanism in the heme-dependent chlorite dismutase, *Biochemistry 52*, 2013, 6982-6994.

[30] S. Sun, Z.S. Li, S.L. Chen, A dominant homolytic O-Cl bond cleavage with low-spin triplet-state Fe(IV)=O formed is revealed in the mechanism of heme-dependent chlorite dismutase, *Dalton Trans 43*, 2014, 973-981.

[31] J.M. Keith, M.M. Abu-Omar, M.B. Hall, Computational investigation of the concerted dismutation of chlorite ion by water-soluble iron porphyrins, *Inorg Chem 50*, 2011, 7928-7930.

[32] J.-X. Su, S.-L. Chen, Significant electron transfer in heme catalysis: The case of chlorite dismutase, *J Catal 348*, 2017, 40-46.

[33] H.C. Yeh, G.J. Gerfen, J.S. Wang, A.L. Tsai, L.H. Wang, Characterization of the peroxidase mechanism upon reaction of prostacyclin synthase with peracetic acid. Identification of a tyrosyl radical intermediate, *Biochemistry 48*, 2009, 917-928.

[34] S.A. Adediran, A.-M. Lambeir, Kinetics of the reaction of compound II of horseradish peroxidase with hydrogen peroxide to form compound III, *Eur J Biochem 186*, 1989, 571-576.

[35] J.N. Rodriguez-Loepz, D.J. Lowe, J. Hernandez-Ruiz, A.N.P. Hiner, F. Garcia-Canovas, R.N.F. Thorneley, Mechanism of Reaction of Hydrogen Peroxide with Horseradish Peroxidase: Identification of Intermediates in the Catalytic Cylce, *J Am Chem Soc 123*, 2001, 11838-11847.

[36] I. Yamazaki, L.H. Piette, Mechanism of free radical formation and disappearance during the ascorbic acid oxidase and peroxidase reactions, *Biochim Biophys Acta 50*, 1961, 62-69.

[37] P.L. Hagedoorn, D.C. de Geus, W.R. Hagen, Spectroscopic characterization and ligand-binding properties of chlorite dismutase from the chlorate respiring bacterial strain GR-1, *Eur J Biochem 269*, 2002, 4905-4911.

[38] D.M. Freire, M.G. Rivas, A.M. Dias, A.T. Lopes, C. Costa, T. Santos-Silva, S. Van Doorslaer, P.J. Gonzalez, The homopentameric chlorite dismutase from *Magnetospirillum* sp, *J Inorg Biochem 151*, 2015, 1-9.

[39] J.M. Berg, J.L. Tymoczko, L. Stryer, The Michaelis-Menten Model Accounts for the Kinetic Properties of Many Enzymes, 8.4, *Biochemistry*, 2002, New York: W. H. Freeman.

[40] A. Cornish-Bowden, Fundamentals of Enzyme Kinetics. 2012, Weinheim, Germany: WILEY-VCH Verlag GmbH & Co. KGaA.

[41] Slide Player, 2014, Transition state diagram, Retrieved 28/05/2019, from https://slideplayer.com/slide/4440669/.

[42] S. Mitic, S. de Vries, Rapid mixing techniques for the study of enzyme catalysis, 1.22, 514-532, *Comprehensive Biophyscis*, 2012, Elsevier.

[43] S. Mitic, M.J.F. Strampraad, W.R. Hagen, S. de Vries, Microsecond time-scale kinetics of transient biochemical reactions, *PLoS One 12*, 2017, e0185888.

[44] A.V. Cherepanov, S. De Vries, Microsecond freeze-hyperquenching: development of a new ultrafast micro-mixing and sampling technology and application to enzyme catalysis, *Biochim Biophys Acta 1656*, 2004, 1-31.

[45] F.G.M. Wiertz, Electron trasnfer and proton pumping pathways in cytochrome aa3, *(Dissertation)*, 2008, Delft University of Technology.

[46] D.M. Murphy, EPR (Electron Paramagnetic Resonance) Spectroscopy of Polycrystalline Oxide Systems, 1, 1-50, *Metal Oxide Catalysis*, 2009, WILEY-VCH Verlag GmbH & Co. KGaA.

[47] W.R. Hagen, EPR Spectroscopy, 3, 53-75, *Practical Approaches to Biological Inorganic Chemistry*, 2013, Elsevier.

[48] Commons Wiki M. Ryazanov, 2011, EPR lines, Retrieved 28/05/2019, from https://commons.wikimedia.org/wiki/File:EPR_lines.png.

[49] M.J. Benecky, J.E. Frew, N. Scowen, P. Jones, B.M. Hoffman, EPR and ENDOR detection of compound I from Micrococcus lysodeikticus catalase, *Biochemistry 32*, 1993, 11929-11933.

[50] S. Yu, S. Girotto, X. Zhao, R.S. Magliozzo, Rapid formation of compound II and a tyrosyl radical in the Y229F mutant of *Mycobacterium tuberculosis* catalase-peroxidase disrupts catalase but not peroxidase function, *J Biol Chem 278*, 2003, 44121-44127.

[51] E.R. Henry, J. Hofrichter, Singular value decomposition: Application to analysis of experimental data, 129-192, *Methods Enzymol*, 1992, Academic Press.

[52] K.A. Johnson, Chapter 23 Fitting Enzyme Kinetic Data with KinTek Global Kinetic Explorer, *Methods Enzymol 467*, 2009, 601-626.

[53] M.J. Kosinski, U. Rinas, J.E. Bailey, Isopropyl-β-d-thiogalactopyranoside influences the metabolism of *Escherichia coli*, *Appl Microbiol Biotechnol 36*, 1992, 782-784.

[54] C.H. Schein, M.H.M. Noteborn, Formation of Soluble Recombinant Proteins in *Escherichia Coli* is Favored by Lower Growth Temperature, *Bio/Technology 6*, 1988, 291-294.

[55] R. Hortsch, D. Weuster-Botz, Growth and recombinant protein expression with *Escherichia coli* in different batch cultivation media, *Appl Microbiol Biotechnol 90*, 2011, 69-76.

[56] T.L. Poulos, Heme Enzyme Structure and Function, *Chem Rev 114*, 2014, 3919-3962.

[57] K.E. Kram, S.E. Finkel, Rich Medium Composition Affects *Escherichia coli* Survival, Glycation, and Mutation Frequency during Long-Term Batch Culture, *Appl Environ Microbiol 81*, 2015, 4442-4450.

[58] D.Z. Mokry, A. Nadia-Albete, M.K. Johnson, G.S. Lukat-Rodgers, K.R. Rodgers, W.N. Lanzilotta, Spectroscopic evidence for a 5-coordinate oxygenic ligated high spin ferric heme moiety in the *Neisseria meningitidis* hemoglobin binding receptor, *Biochim biophys acta 1840*, 2014, 3058-3066.

[59] M.T. Neves-Petersen, S. Klitgaard, A.S.L. Carvalho, S.B. Petersen, M.R. Aires de Barros, E.P. e Melo, Photophysics and Photochemistry of Horseradish Peroxidase A2 upon Ultraviolet Illumination, *Biophys J 92*, 2007, 2016-2027.

[60] Y.A. Vladimirov, D.I. Roshchupkin, E.E. Fesenko, Photochemical reactions in amino acids residues and inactivation of enzymes during U.V.-irradiation. A Review, *Photochem Photobiol 11*, 1970, 227-246.

[61] Q. Wu, G. Balakrishnan, A. Pevsner, T.G. Spiro, Histidine Photodegradation during UV Resonance Raman Spectroscopy, *J Phys Chem 107*, 2003, 8047-8051.

[62] N. Grotjohann, A. Janning, R. Eising, In Vitro Photoinactivation of Catalase Isoforms from Cotyledons of Sunflower (*Helianthus annuusL*.), *Arch Biochem Biophys 346*, 1997, 208-218.

[63] B.R. Streit, B. Blanc, G.S. Lukat-Rodgers, K.R. Rodgers, J.L. DuBois, How Active-Site Protonation State Influences the Reactivity and Ligation of the Heme in Chlorite Dismutase, *J Am Chem Soc 132*, 2010, 5711-5724.

[64] S. Hofbauer, K. Gysel, M. Bellei, A. Hagmuller, I. Schaffner, G. Mlynek, J. Kostan, K.F. Pirker, H. Daims, P.G. Furtmuller, G. Battistuzzi, K. Djinovic-Carugo, C. Obinger, Manipulating conserved heme cavity residues of chlorite dismutase: effect on structure, redox chemistry, and reactivity, *Biochemistry 53*, 2014, 77-89.

[65] N.E. Good, G.D. Winget, W. Winter, T.N. Connolly, S. Izawa, R.M.M. Singh, Hydrogen Ion Buffers for Biological Research*, *Biochemistry 5*, 1966, 467-477.

[66] W. D Hewson, L. P Hager, Oxidation of horseradish peroxidase compound II to compound I, *J Biol Chem 254*, 1979, 3192-3196.

[67] A.N.P. Hiner, J.I. Martínez, M.B. Arnao, M. Acosta, D.D. Turner, E. Lloyd Raven, J.N. Rodríguez-López, Detection of a tryptophan radical in the reaction of ascorbate peroxidase with hydrogen peroxide, *Eur J Biochem 268*, 2001, 3091-3098.

[68] W.R. Patterson, T.L. Poulos, D.B. Goodin, Identification of a Porphyrin .pi. Cation Radical in Ascorbate Peroxidase Compound I, *Biochemistry 34*, 1995, 4342-4345.

[69] J.M. Mauro, L.A. Fishel, J.T. Hazzard, T.E. Meyer, G. Tollin, M.A. Cusanovich, J. Kraut, Tryptophan-191 to phenylalanine, a proximal-side mutation in yeast cytochrome c peroxidase that strongly affects the kinetics of ferrocytochrome c oxidation, *Biochemistry 27*, 1988, 6243-6256.

[70] C. Jakopitsch, H. Spalteholz, P.G. Furtmüller, J. Arnhold, C. Obinger, Mechanism of reaction of horseradish peroxidase with chlorite and chlorine dioxide, *J Inorg Biochem 102*, 2008, 293-302.

[71] J.-Y. Chang, Thrombin specificity, *Eur J Biochem 151*, 1985, 217-224.

[72] B. Srour, M.J.F. Strampraad, W.R. Hagen, P.L. Hagedoorn, Refolding kinetics of cytochrome c studied with microsecond timescale continuous-flow UV-vis spectroscopy and rapid freeze-quench EPR, *J Inorg Biochem 184*, 2018, 42-49.

[73] Lab Training, D. Bhanot, 2015, Benefits of Photodiode Array Detection over conventional Scanning detection, Retrieved 08/06/2019, from http://lab-training.com/2015/07/13/benefits-of-photodiode-array-detection-over-conventional-scanning-detection/.

[74] CHROMacademy, Optical Arrangements of UV-visible Spectrophotometers, Retrieved 08/05/2019, from https://www.chromacademy.com/lms/sco736/10-Optical-Arrangements-of-UV-visible-Spectrophotometers.html?fChannel=22&fCourse=97&fSco=736&fPath=sco736/10-Optical-Arrangements-of-UV-visible-Spectrophotometers.html.

[75] H.B. Dunford, Horseradish Peroxidase. I. The Native Enzyme, Compounds I and II, Their Structures, and Their Cycle, 3, 13-39, *Peroxidases and Catalases: Biochemistry, Biophysics, Biotechnology and Physiology*, 2010, New York: Wiley-CH.

Appendices

Appendix A

Equation 1: Formula for calculating the volumetric activity

$$(Slope - NE) * \frac{c(O_{2,max})}{O_{2,max}} * \left(\frac{V_{reaction} + V_{enzyme}}{V_{enzyme}} * DF\right)$$

$Slope = Slope\ measured\ by\ the\ electrode$ $[V\ min^{-1}]$
$NE = Non - enzymatic\ diffusion\ of\ oxygen\ into\ the\ buffer$ $[V\ min^{-1}]$
$c(O_{2,max}) = Maximum\ amount\ of\ oxygen\ that\ can\ be\ dissolved\ in\ water\ (298\ K)$ $[\mu M]$
$O_{2,max} = Voltage\ difference\ between\ 100\%\ oxygen\ and\ 0\%\ oxygen\ dissolved$ $[V]$
$V_{reaction} = Volume\ of\ the\ reaction\ vessel$ $[mL]$
$V_{enzyme} = Volume\ of\ added\ enzyme$ $[mL]$
$DF = Dilution\ factor$

Equation 2: Formula for calculating a first-order rate constant at 9°C given a first-order rate constant at 29°C (Adapted from [72])

1. Under the assumption that the $\Delta G^{\dagger}$ does not change with temperature we can write for each intermediate at two different temperatures T_1 and T_2:

$$-RT_1 \ln\left(\frac{k_1}{\frac{k_B * T_1}{h}}\right) = -RT_2 \ln\left(\frac{k_2}{\frac{k_B * T_2}{h}}\right)$$

2. Rewrite the equation to:

$$k_1 = \frac{k_B * T_1}{h} * \left(\frac{k_2 * h}{k_B * T_2}\right)^{\frac{T_2}{T_1}}$$

$k_B = Boltzman\ constant\ with\ 1.0381 * 10^{-23}\ \frac{J}{K}$
$h = Planck\ constant\ with\ 6.626 * 10^{-34}\ J * s$
$T_1 = 9°C$
$T_2 = 29°C$
$k_2 = first - order\ rate\ constant\ at\ 29°C$

Appendix B

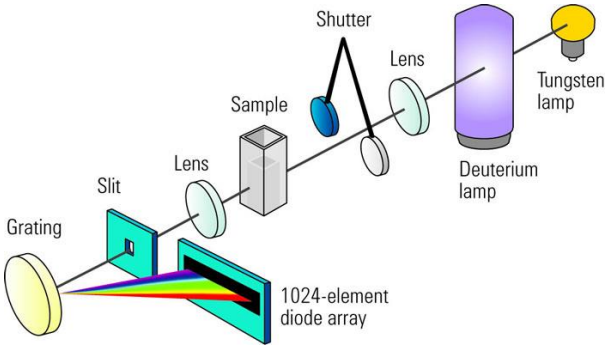

Supp. Figure 1. Set-up of a photo-diode array spectrophotometer. Taken from [73].

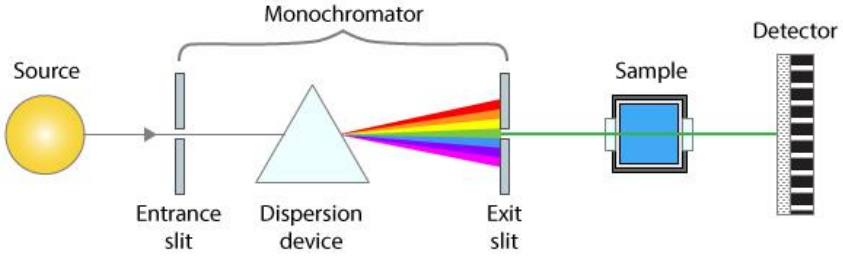

Supp. Figure 2. Set-up of a monochromator. Taken from [74].

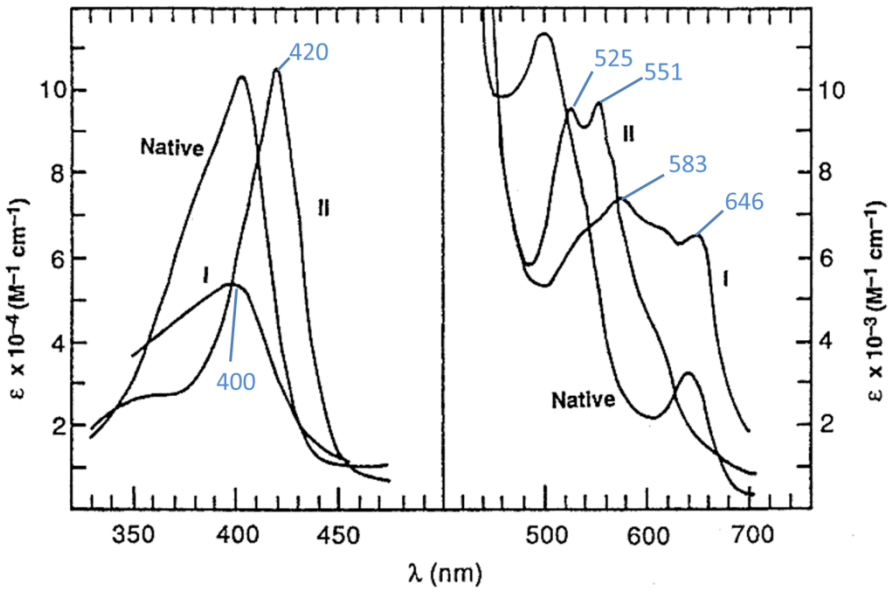

Supp. Figure 3. Compound I and Compound II spectra of Horseradish peroxidase. Adapted from [75].

Appendix C

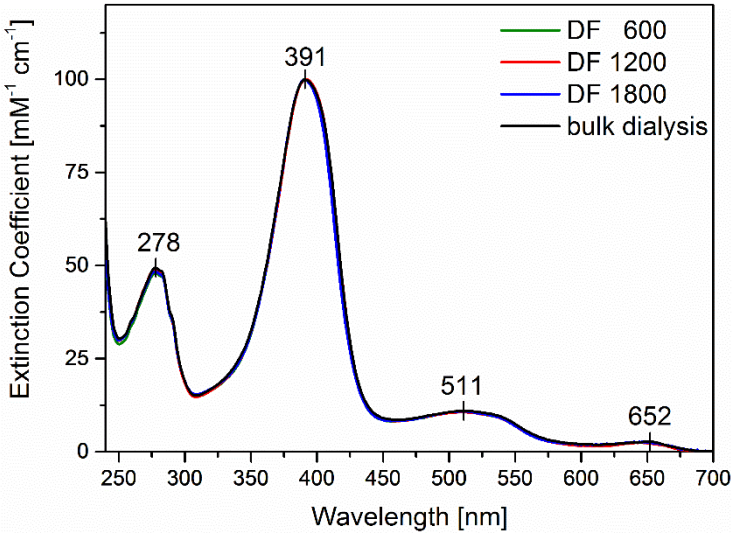

Supp. Figure 4. UV-Vis spectra of a small scale test dialysis to determine the effect of the imidazole removal on the UV-Vis spectrum of *Ao*Cld. 1 mL of *Ao*Cld (8 mg mL^{-1}) each have been dialysed to a dilution factor (DF) of 600 (green), 1200 (red), and 1800 (blue). The spectrum after the bulk dialysis (black) is present as a reference. UV-Vis spectra were obtained with 10 µM *Ao*Cld in 100 mM KPi buffer, pH 7, at 21°C.

Supp. Table 1. Purification table from the fermentation 2 batch 2.

sample	Volume [mL]	protein conc. [mg mL^{-1}]	Activity [$\cdot 10^4$ U mL^{-1}]	Total Activity [$\cdot 10^6$ U]	Specific Activity [U mg^{-1}]	Purification [fold]	Yield [%]	Rz [A_{391nm}/A_{280nm}]
cell lysate	1280	7.87	2.2 ± 0.1	28.8	2856	1.0	100	-
Ni-NTA	132	17.57	15.5 ± 0.2	20.5	8838	3.1	71	1.05
Desalted	130	13.44	12.8 ± 0.5	16.7	9543	3.3	58	1.76
PD10	210	6.87	6.7 ± 0.5	14.2	9821	3.4	49	1.80
Dialysed	170	7.91	6.7 ± 0.2	11.5	8515	3.0	40	2.04

Total protein conc.: 170 mL * 7.91 mg mL^{-1} = 1343 mg

Total cell wet weight: 106 g

Yield: 1343 mg/106 g = 12.7 mg protein per g cell wet weight

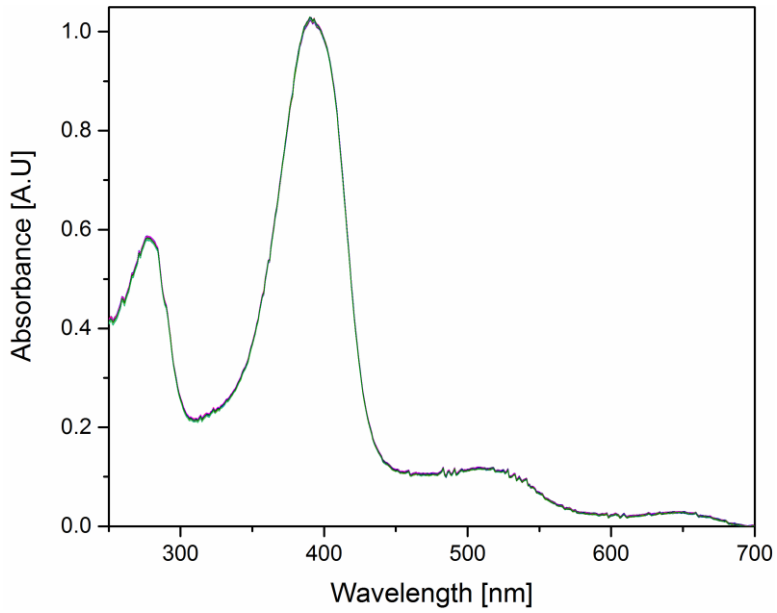

Supp. Figure 5. Spectra of *Ao*Cld in a Cary 60 spectrophotometer (monochromator). Raw data of 50 spectra are shown as representatives from the measurement of 10 µM *Ao*Cld in Milli-Q. Spectra were taken at 21°C. Enzyme-water mixture was stirred at 650 rpm.

.

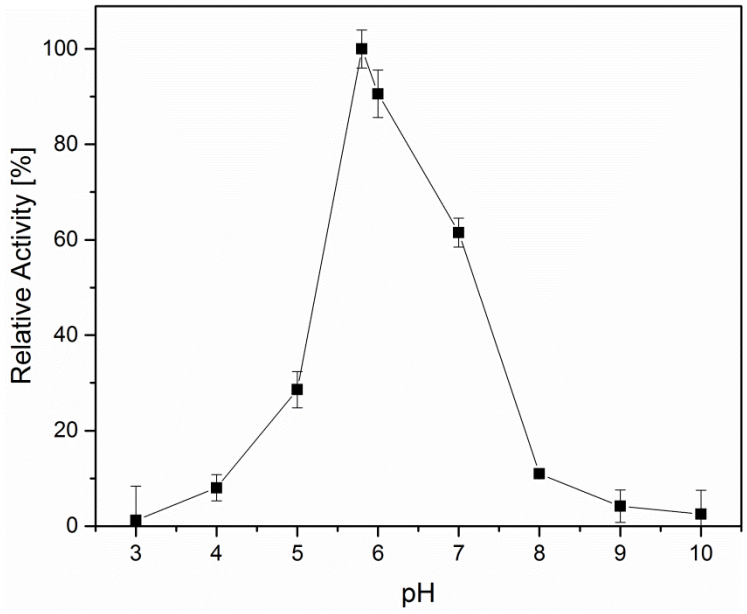

Supp. Figure 6. pH optimum curve for *Ao*Cld. Specific activities were measured in 100 mM citrate-phosphate buffer (pH 3 – 5.8), 100 mM KPi buffer (pH 5.8 – 8), 100 mM Tris buffer (pH 8 – 9), and CHES buffer (pH 9 – 10), 1 mM sodium chlorite, 88 pM – 1.3 nM *Ao*Cld, 20°C. Experiments were performed in triplicates. Data obtained by Durga Mahor, 2019. Printed with permission.

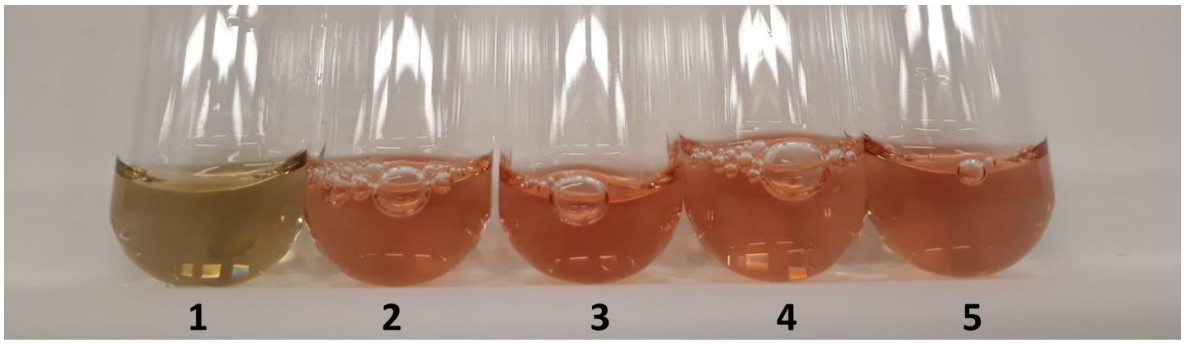

1 Acetate buffer pH 5
2 Citrate (phosphate) buffer pH 5
3 Citrate (sodium) buffer pH 5
4 Phosphate buffer pH 7
5 Tris buffer pH 8

Supp. Figure 7. Colour change upon incubation with acetate buffer. Acetate ions bind to the heme moiety of *Ao*Cld and change its red colour (2-5) to a greenish colour (1).

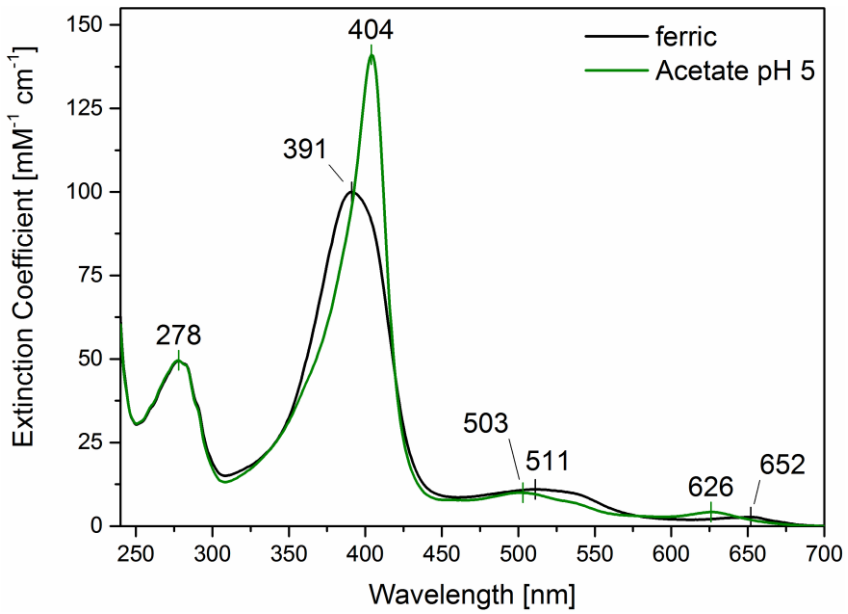

Supp. Figure 8. Spectral change of *Ao*Cld in acetate buffer. 10 µM *Ao*Cld was dissolved in 100 mM KPi, pH 7 (ferric) and 100 mM acetate buffer, pH 5 (green). Spectra were taken at 21°C.

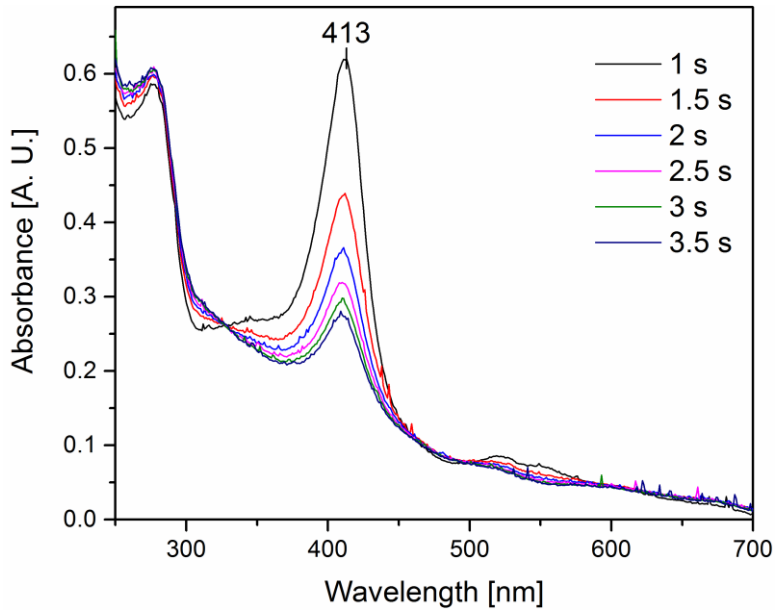

Supp. Figure 9. Spectral changes of *Ao*Cld mixed with PAA (raw data). 20 µM *Ao*Cld (10 µM end concentration) was mixed 1:1 with PAA in a Cary 60 spectrophotometer, 20°C, and spectra were started after ~1 s after mixing. Enzyme-PAA mixture was stirred at 650 rpm.

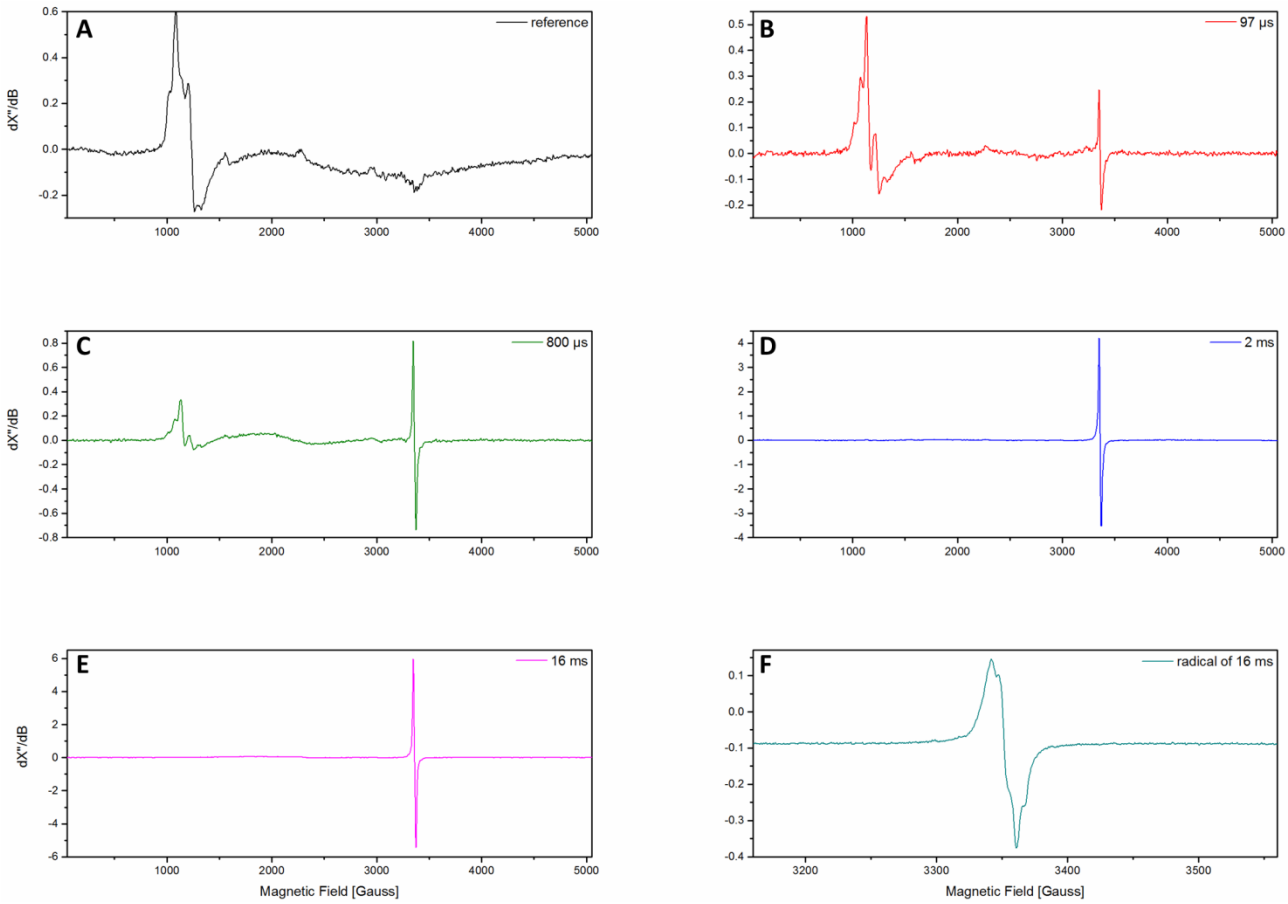

Supp. Figure 10. EPR spectra of the MHQ prepared samples with PAA and *Ao*Cld. 1.5 mM PAA and 500 µM *Ao*Cld, both dissolved in 100 mM KPi, pH 7, were mixed at 9°C and frozen rapidly. A – 500 µM *Ao*Cld and 100 mM KPi buffer, pH 7, have been mixed for a reference spectrum. The reaction between PAA and *Ao*Cld was quenched 97 µs (B), 800 µs (C), 2 ms (D), and 16 ms (E) after mixing. F shows the scan of the radical at 16 ms after mixing (4x average). EPR spectra were obtained with microwave frequency 9.4 GHz, microwave power 20 mW (0.2 mW for F), modulation frequency 100 kHz, modulation amplitude 10 G (2 G for F), and temperature 20 K.

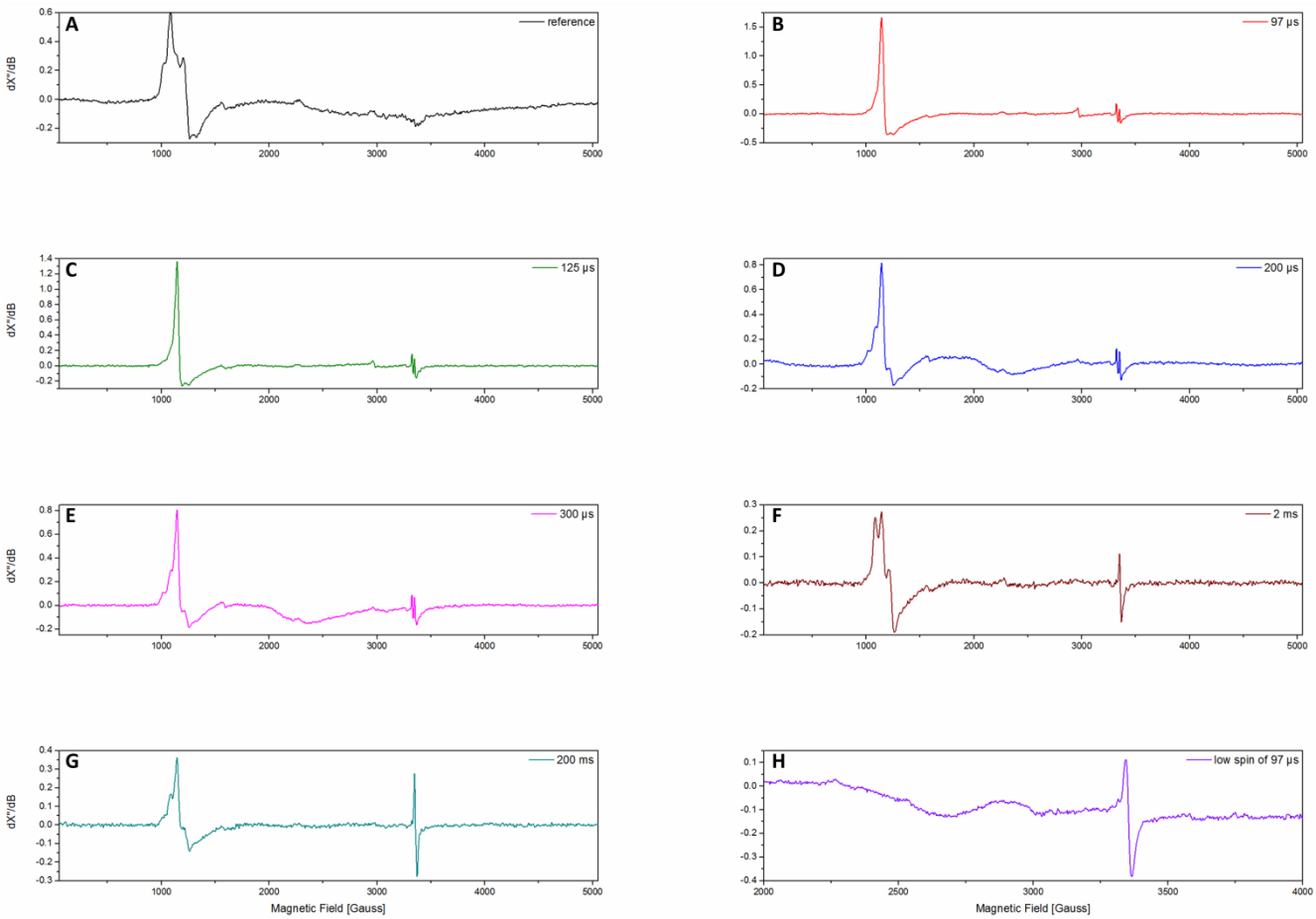

Supp. Figure 11. EPR spectra of the MHQ prepared samples with sodium chlorite and *Ao*Cld. 75 mM sodium chlorite and 500 µM *Ao*Cld, both dissolved in 100 mM KPi, pH 7, were mixed at 9°C and frozen rapidly. A – 500 µM *Ao*Cld and 100 mM KPi buffer, pH 7, have been mixed for a reference spectrum, reaction between sodium chlorite and *Ao*Cld was quenched 97 µs (B), 125 µs (C), 200 µs (D), 300 µs (E), 2 ms (F), and 200 ms (G) after mixing. H shows the narrow scan of the low spin signal at 97 µs after mixing (4x average). EPR spectra were obtained with microwave frequency 9.4 GHz, microwave power 20 mW (0.2 mW for H), modulation frequency 100 kHz, modulation amplitude 10 G (2 G for H), and temperature 20 K.